Contributions to Mineralogy and Petrology (2022) 177:98
https://doi.org/10.1007/s00410-022-01954-1

ORIGINAL PAPER

Modelling hydrogen mobility in forsterite as diffusion coupled to inter-site reaction

Michael C. Jollands[1,2] · Joshua Muir[3] · José Alberto Padrón-Navarta[4,5] · Sylvie Demouchy[5,6]

Received: 22 April 2021 / Accepted: 8 August 2022 / Published online: 3 October 2022

Abstract

Whilst the diffusivity of hydrogen (H) in forsterite (Mg_2SiO_4) has been extensively studied, there still remain some puzzling observations. Firstly, experiments measuring ostensibly the same process have provided different results in terms of diffusion coefficients. Secondly, despite H diffusion in forsterite generally being associated with diffusion of M-vacancies charge compensated by $2H^+$, a plethora of H-bearing point defects have been observed, including those associated with Si vacancies, trivalent cations and tetravalent cations in the form of so-called 'clinohumite-type' point defects. This has been tentatively associated with some form of inter-site reaction, such as one in which a M-site vacancy associated with $2H^+$ reacts with tetrahedrally coordinated Ti^{4+}. Equivalent reactions can be constructed to form all point defects mentioned above. Here, we present a series of numerical models in which these processes are simulated. In the models, the mobility of H is described using a diffusion coefficient (D^*) for the hydrogenated M-site vacancies and an equilibrium constant (K) for the relevant inter-site reaction(s). Reevaluation of published data shows that the extracted D^* and K values are consistent between some different datasets, even in situations where the phenomenological (chemical) diffusion coefficient $\tilde{D}$, extracted simply using solutions of Fick's second law, did not agree. The 'true' mobility (D^*) of the M-site vacancy associated with $2H^+$ must be between 1 and 2 orders of magnitude greater than previously determined $\tilde{D}$ in order to form measurable profiles of all point defects observed by vibrational spectroscopy. Density functional theory calculations of the K of each of the inter-site reactions implemented in our model show good agreement (within an order of magnitude) with those determined experimentally for the reactions forming 'clinohumite-type' defects, but considerable disagreement (~ 3 orders of magnitude) for the defects involving trivalent cations, potentially due to assumptions related to binding of different components within individual defects. Overall, the first-order implication is that H diffusion profiles that we observe in natural and experimental samples are unlikely to be formed by simple diffusion alone. These models provide a new methodological framework for further understanding of complex ionic diffusion mechanisms in olivine and the other nominally anhydrous minerals.

Keywords Nominally anhydrous minerals · Olivine · Diffusion · Hydrogen

Communicated by Hans Keppler.

✉ Michael C. Jollands
mjolland@gia.edu

[1] Lamont-Doherty Earth Observatory, 61 Rt. 9W, Palisades, NY 10964, USA

[2] Gemological Institute of America, 50 W. 47th St, New York, NY 10036, USA

[3] State Key Laboratory of Ore Deposit Geochemistry, Institute of Geochemistry, Chinese Academy of Sciences, 99 West Lincheng Road, Guiyang 550081, Guizhou, China

[4] Instituto Andaluz de Ciencias de la Tierra, CSIC-Universidad de Granada, Av. de las Palmeras, 4, 18100 Armilla, Spain

[5] Géosciences Montpellier, Université de Montpellier, CNRS, 34095 Montpellier, France

[6] Laboratoire Magmas et Volcans, Université Clermont Auvergne, CNRS, IRD, OPGC, 6300 Clermont-Ferrand, France

Introduction

In the upper mantle, the small amount of hydrogen incorporated into nominally anhydrous minerals has been shown to affect various physio-chemical properties (see Zhang and Xia 2021, for a comprehensive review) although the extent of the effects is still debated to some extent. Studies have focussed on electrical conductivity (Dai and Karato 2014, 2020; Karato 1990; Liu et al. 2019; Yang et al. 2012; Yoshino et al. 2009; Zhao and Yoshino 2016), plastic deformation (Chen et al. 1998, 2006; Demouchy et al. 2012; Faul et al. 2016; Katayama and Karato 2008; Mackwell et al. 1985; Mei and Kohlstedt 2000; Tielke et al. 2017), seismic attenuation (Aizawa et al. 2008; Cline et al. 2018; Karato and Jung 1998) and major element diffusion (Costa and Chakraborty 2008; Fei et al. 2018; Hier-Majumder et al. 2005; Wang et al. 2004; Zhang et al. 2019). The hydrogen is normally bonded to structural oxygen, forming hydroxyl groups (OH^-). It is generally thought to diffuse as protons (H^+) and is conventionally quantified as 'water', given that its solubility is a function of water fugacity, fH_2O (Kohlstedt et al. 1996; Lu and Keppler 1997; Rauch and Keppler 2002). The polarisation, lengths and stretching frequencies of the O–H bonds are sensitive to their local environment, for example, an OH group adjacent to a tetrahedral vacancy has different characteristics to one adjacent to an octahedral vacancy (e.g., Balan et al. 2011). Fourier transform infrared (FTIR) spectroscopy allows these different O–H bonds to be distinguished and with detailed experimental, computational and petrological studies (e.g., Berry et al. 2005; Blanchard et al. 2017; Crépisson et al. 2014b; Le Losq et al. 2019; Lemaire et al. 2004; Matveev et al. 2001; Padrón-Navarta and Hermann 2017; Tollan et al. 2017), they can be assigned to specific H-bearing point defects.

Much attention has been devoted to unravelling the concentration, speciation and mobility of hydrogen in olivine especially, which now ranks amongst the most intensively and extensively studied diffusion systems in the Earth sciences. However, almost every experimental hydrogen diffusion study to date has assumed that diffusion can be described simply using analytical solutions or numerical approximations of Fick's second law. This is entirely reasonable from the phenomenological perspective, but does not explain the diversity of OH-bearing point defects observed following H in-diffusion experiments, nor the considerable discrepancies (orders of magnitude) between different studies measuring ostensibly the same process. In this contribution, we attempt to resolve these problems by considering that hydrogen diffusion in olivine (in this case, pure or nominally pure forsterite) is best described not as a single, simple mechanism of diffusion, but rather as diffusion accompanied and to some extent rate-limited, by inter-site redistribution of hydrogen. Models are constructed, tested and evaluated, which go some way towards reconciling different laboratory studies and discrepancies between theory and observation.

Background

Hydrogen diffusion: rates and mechanisms in olivine

Hydrogen diffusion in olivine ($(Mg, Fe)_2SiO_4$) has been the subject of three decades of experimental research. Experiments have been conducted over a wide temperature range (~ 500–1300 °C), with around six orders of magnitude difference between the lowest and highest measured diffusivities at 1000 °C. The difference increases with decreasing temperature, potentially exceeding ten orders of magnitude at 700 °C, albeit with considerable down-temperature extrapolation of experimental diffusion coefficients. The prevailing explanation is that these major differences between diffusivities are due to the existence of at least three fundamentally different diffusion mechanisms.

The highest measured diffusivities, usually with the lowest activation energies (100–200 kJ mol^{-1}) are ascribed to the exchange of protons for polarons, where 'polaron' is used loosely, to describe a positively charged hole that would otherwise be occupied by an electron. Proton hopping is therefore enabled by the reduction of Fe^{3+} to Fe^{2+} (Kohlstedt and Mackwell 1998; Mackwell and Kohlstedt 1990; Barth et al. 2019; Ferriss et al. 2018; Demouchy and Mackwell 2006; Jollands et al. 2019; Li et al. 2022). These diffusivities are consistently highest parallel to the [100] direction, although the reason for this particular anisotropy is not yet clear. Hydrogen–deuterium exchange experiments in Fe-bearing olivine (Novella et al. 2017; Sun et al. 2019; Du Frane and Tyburczy 2012), which aim to extract the self diffusion coefficient of H, generally show similar diffusivities to this rapid 'proton−polaron' exchange. This is in general agreement with previous data from Kohlstedt and Mackwell (1998), who suggest that the measured (a.k.a. chemical or exchange) diffusivities ($\tilde{D}$), i.e., those that would be extracted from directly fitting an experimental diffusion profile, are related to the self-diffusion coefficient of H (D_H) and the diffusivity of the polaron (D_P) by $D_P \gg 2D_H \approx \tilde{D}$. The derivation of this relationship is detailed in Kohlstedt and Mackwell (1999). However, the uncertainties associated with both the proton–polaron exchange diffusivities and those associated with H self-diffusion, are too large to confirm or refute the $2D_H \approx \tilde{D}$ relationship. As of yet, there are no published studies of hydrogen–deuterium (^2H) exchange

in end-member forsterite (Mg_2SiO_4). However, unpublished results presented by Ingrin and Kohn (2008) and Ingrin and Blanchard (2006) using both natural and synthetic forsterite, show that the relevant diffusivity is lower than that of hydrogen–deuterium exchange in natural olivine and similar to that of the metal vacancy mechanism (described next). As with the hydrogen–deuterium exchange experiments in natural olivine, the equivalent diffusivity in pure forsterite is highest parallel to [100] direction, thus it is unlikely that the observed anisotropy is related to the presence of Fe.

In the second group, the diffusivities are lower, with a higher activation energy than the first mechanism (200–250 kJ mol^{-1}) and associated with the highest diffusivity parallel to [001]. These are generally accepted to relate to H^+ diffusion associated with M-site (M = metal) vacancies, whereby a M-site vacancy is charge balanced by $2H^+$ and exchanges places with a cation (Mg^{2+} in pure forsterite) in its usual site (Demouchy and Mackwell 2003, 2006; Ingrin and Blanchard 2006; Jollands et al. 2016b; Kohlstedt and Mackwell 1998; Padrón-Navarta et al. 2014). Kohlstedt and Mackwell (1998) suggest that the measured diffusivity (again $\tilde{D}$) is related to the self-diffusion coefficient of H, rate-limited by the diffusivity of the M-site vacancy (D_{V_M}) via $D_H \gg 3\, D_{V_M} \approx \tilde{D}$.

The anisotropy is likely explained by the spacing of M sites in the olivine structure—the M1 sites form a chain parallel to [001], which provides the shortest hop and thus highest diffusivity. The same anisotropy is also observed in Mg tracer diffusion experiments in forsterite (Chakraborty et al. 1994; Jollands et al. 2020), as well as in other experiments studying diffusion of M1-ordered cations in olivine (Chakraborty 1997; Dohmen et al. 2007; Dohmen and Chakraborty 2007; Spandler and O'Neill 2010; Zhukova et al. 2014).

The final diffusion mechanism is considerably slower, with a much higher activation energy (> 400 kJ mol^{-1}). This has only been observed once (Padrón-Navarta et al. 2014) in experiments conducted using pure forsterite synthesised in MgO buffered (low silica activity, $aSiO_2$) conditions. Based on the point defects that were inferred by Padrón-Navarta et al. (2014), as well as the high activation energy, this diffusivity was suggested to be associated with exchange of a Si vacancy, charge compensated by $4H^+$, with Si^{4+} in its usual lattice site. It is not known whether this mechanism is anisotropic, but comparison with Si tracer diffusion experiments (Costa and Chakraborty 2008) suggests that this should be either weakly anisotropic or isotropic. This mechanism may be important for deformation of olivine under hydrous conditions as it should facilitate mass transfer of Si via a vacancy mechanism, but this diffusivity may be less relevant if considering, for example, retentivity of hydrogen in olivine on ascent from the mantle in xenoliths or diffusion chronometry at magmatic temperatures. The presence of Fe appears to open up a pathway that allows H to be rapidly lost (minutes to weeks at < 1000 °C) from these defects (Jollands et al. 2019), although, paradoxically, metamorphic Fe-bearing olivine from Zermatt, Switzerland, appears to have retained water associated with this defect for millions of years (Kempf and Hermann 2018; Kempf et al. 2020).

Predictions versus experimental observations

In the following, and throughout, defects are described using Kröger–Vink notation (Kröger and Vink 1956). We assign H to a lattice site, rather than describing it as interstitial or associating it with an OH group. This is done for brevity only; further descriptions are presented in Table 1. Vacancies are denoted *V*, italicised. We describe diffusion experiments as H-in and H-out, referring to the main flux direction. This is for consistency only; such experiments have also been described as 'hydrogenation'/'dehydrogenation', 'hydration'/'dehydration' and 'hydroxylation'/'dehydroxylation'.

Herein, we consider only pure/nominally pure/trace-element-doped forsterite. If the prevailing explanation, where the highest diffusivities are ascribed to proton-polaron exchange (Kohlstedt and Mackwell 1998; Mackwell and Kohlstedt 1990; Demouchy and Mackwell 2006) is correct, then this mechanism should not be available in pure, Fe-free forsterite. Therefore, within our current understanding, in pure forsterite, hydrogen should only have two diffusion mechanisms, one occurring via $(2H)_M^\times$ exchanging with $Mg_M^\times$ and the other being the exchange of $(4H)_{Si}^\times$ for $Si_{Si}^\times$. This leads to two predictions. Firstly, H in-diffusion experiments should only contain, at a maximum, two OH-bearing defects, being $(4H)_{Si}^\times$ and $(2H)_M^\times$. In fact, according to Padrón-Navarta et al. (2014), the diffusivity associated with $(4H)_{Si}^\times$ is so low that at the temperature–time conditions of all previous H in-diffusion experiments, only $(2H)_M^\times$ should be observed given the relatively poor spatial resolution of transmission FTIR spectroscopy (10 s µm, e.g., Ni and Zhang 2008). Secondly, in H-out diffusion experiments, only $(2H)_M^\times$ and $(4H)_{Si}^\times$ should be mobile, with the latter showing considerably lower mobility than the former. Neither of these predictions are supported by the data, as is described herein.

Firstly, H-in experiments show a plethora of point defects (Table 1, Fig. 1). The first H-in study using forsterite was conducted by Demouchy and Mackwell (2003), who annealed nominally pure, synthetic forsterite at 900–1100 °C, 0.2–1.5 GPa, in the presence of enstatite (powder of 90% forsterite, 10% enstatite), aqueous fluid and either Ni–NiO or Fe–FeO mixes to buffer the $aSiO_2$, fH_2O and oxygen fugacity (fO_2), respectively. The starting crystals were pre-annealed at 1300 °C for 20 h to ensure that they were water-free, with the implicit assumption that this also led to an equilibration of the anhydrous point defect

Table 1 OH-bearing defects observed in previous studies using pure or trace element-doped forsterite, shaded cells mean that the defect was observed in the study

Kröger-Vink			End-member	Short-hand	D03	P14	J16	J21
$(2H)_M^\times$	$\{V_M'' - 2H_i^\bullet\}^\times$	$\{V_M'' - 2(OH)_O^\bullet\}^\times$	MgH_2SiO_4	[Mg]				
$(4H)_{Si}^\times$	$\{V_{Si}'''' - 4H_i^\bullet\}^\times$	$\{V_{Si}'''' - 4(OH)_O^\bullet\}^\times$	$Mg_2H_4O_4$	[Si]				
$\{Al_M^\bullet - H_M'\}^\times$	$\{Al_M^\bullet - V_M'' - H_i^\bullet\}^\times$	$\{Al_M^\bullet - V_M'' - (OH)_O^\bullet\}^\times$	$AlHSiO_4$	[Al-triv]				
$\{Cr_M^\bullet - H_M'\}^\times$	$\{Al_M^\bullet - V_M'' - H_i^\bullet\}^\times$	$\{Cr_M^\bullet - V_M'' - (OH)_O^\bullet\}^\times$	$Cr^{3+}HSiO_4$	[Cr-triv]				
$\{Ti_M^\bullet - H_M'\}^\times$	$\{Ti_M^\bullet - V_M'' - 2H_i^\bullet\}^\times$	$\{Ti_M^\bullet - V_M'' - (OH)_O^\bullet\}^\times$	$Ti^{3+}HSiO_4$	[Ti-triv]				
$\{Cr_M^{\bullet\bullet} - (2H)_{Si}''\}^\times$	$\{Cr_M^{\bullet\bullet} - V_M'' - 2H_i^\bullet\}^\times$	$\{Cr_M^{\bullet\bullet} - V_M'' - 2(OH)_O^\bullet\}^\times$	$MgCr^{4+}H_2O_4$	[CrCH-PD]				
$\{Ti_M^{\bullet\bullet} - (2H)_{Si}''\}^\times$	$\{Ti_M^{\bullet\bullet} - V_M'' - 2H_i^\bullet\}^\times$	$\{Ti_M^{\bullet\bullet} - V_M'' - 2(OH)_O^\bullet\}^\times$	$MgTi^{4+}H_2O_4$	[Ti] or [TiCH-PD]				

population. Following the experiments, they found major, broad bands at 3155 and 3215 cm^{-1} ($(2H)_M^\times$ defect), as well as less intense, sharp bands at 3613, 3579 and 3567 cm^{-1} ($(4H)_{Si}^\times$). These bands showed diffusion profiles with similar length scales, which is not in agreement with the Padrón-Navarta et al. (2014) observation (discussed below) that the diffusivity associated with $(2H)_M^\times$ is orders of magnitude greater than that associated with $(4H)_{Si}^\times$. Their Table 2 also shows the presence of bands at 3344 and 3350 cm^{-1}, which may represent $\{Al_M^\bullet - H_M'\}^\times$ (Berry et al. 2007a).

Later, Jollands et al. (2016b) presented results of H-in experiments, using explicitly Ti-doped forsterite, which was prepared by doping pure synthetic forsterite with Ti, by diffusion, at low fO_2 (~ QFM-5.2, O'Neill 1987) and high temperature (1500 °C) such that Ti was likely to be present mostly as Ti^{3+}, with some minor Ti^{4+}. These were then annealed at 650–1000 °C, 1.5–2.5 GPa along with enstatite or periclase ($aSiO_2$ buffer), aqueous fluid ($aH_2O \approx 1$ at run conditions) and Re–ReO_2 or Ag–Ag_2O (fO_2 buffer). It was assumed that the Ti in the starting material was already present as octahedrally coordinated Ti^{4+} (minor) and Ti^{3+} and tetrahedrally coordinated Ti^{4+} ($\{Ti_M^{\bullet\bullet} - V_M''\}^\times$, $\{2Ti_M^\bullet - V_M''\}^\times$ and $Ti_{Si}^\times$, respectively). The only other aliovalent ion present in the Jollands et al. (2016a, b) experiments at a significant concentration was Al^{3+} (~ 10 wt ppm). Small amounts (10 s wt ppm) of Fe contamination were also introduced, but, given the fO_2 of the Ti-doping step, it is reasonable to assume all Fe was initially present as Fe^{2+}. Following hydration experiments, they observed bands at 3524, 3571 cm^{-1} ($\{Ti_M^{\bullet\bullet} - (2H)_{Si}''\}^\times$), 3164 cm^{-1} ($(2H)_M^\times$) and 3351, 3313 cm^{-1} ($\{Ti_M^\bullet - H_M'\}^\times$). As with the Demouchy and Mackwell (2003) experiments, all bands showed absorbance–distance profiles with similar length scales.

The most recent study comes from Jollands et al. (2021), who annealed Cr-doped forsterite, grown for lasing purposes (e.g., Petričević et al. 1988; Rager et al. 1991) at 750–1300 °C, 0.5–2.5 GPa, with enstatite or periclase, pure water and Re–ReO_2, Ni–NiO, Fe_2O_3–Fe_3O_4, Ag–Ag_2O or graphite to buffer fO_2 . The starting material was assumed to contain at least $\{2Cr_M^\bullet - V_M''\}^\times$ and $Cr_{Si}^\times$ (Cr^{3+} and Cr^{4+}, respectively), but $\{2Al_M^\bullet - V_M''\}^\times$, $\{Al_M^\bullet - Al_{Si}'\}^\times$ and/or $\{Cr_M^\bullet - Al_{Si}'\}^\times$ may have also been present. Following H-in experiments, the samples showed many resolvable peaks (at least 24), with the main peaks being at 3306, 3325 and 3354 cm^{-1} ($\{Cr_M^\bullet - H_M'\}^\times$); 3155 cm^{-1} ($(2H)_M^\times$); 3568, 3579, 3612 cm^{-1} ($(4H)_{Si}^\times$) and 3544, 3572, 3591 cm^{-1} ($\{Cr_M^{\bullet\bullet} - (2H)_{Si}''\}^\times$). The arguments for the presence of a $\{Cr_M^{\bullet\bullet} - (2H)_{Si}''\}^\times$ defect are detailed in Jollands et al. (2021) and we assume here that their designation is correct.

Libowitzky and Beran (1995) presented the results of H-out and hydrogen–deuterium exchange experiments using near-pure natural forsterite (0.25 wt% Fe). Their starting material was from a skarn deposit (Pamir, Tajikistan) and contained bands at 3674, 3640, 3598, 3570, 3592 and 3535 cm^{-1}, all of which are consistent with hydrogen associated with Si vacancies and F^- (Crépisson et al. 2014a). These crystals were heated for 24 h at 1000, 1100, 1200 and 1300 °C in air. Some bands were found to be more resistant to annealing than others, e.g., the 3674, 3535 and 3514 cm^{-1} bands grew in absorbance relative to their initial state, after heating at 1000 °C. Experiments conducted in a Ar–$^2H_2$ atmosphere showed complete exchange of OH for O^2H. Libowitzky and Beran (1995) provide insufficient data to allow quantitative descriptions of their results, so these experiments will not be discussed here. However, in light of new understanding, repeating these studies using modern analytical techniques considering diffusion associated with F^-–OH^- defects could be extremely enlightening, given the potential importance of olivine as a fluorine host in the mantle (Grützner et al. 2017; Joachim et al. 2017), at least in situations where a clinohumite phase is not stabilised (Garrido et al. 2005; Hermann et al. 2007; Hughes and Pawley 2019).

Padrón-Navarta et al. (2014) presented the results of H-out experiments using Ti-doped forsterite. Single crystals of Ti- and H-bearing forsterite were grown at 1400 °C, 2 GPa, in both Ti-doped and MgO-excess experiments (synthesis protocol is reported in Petersen (2013), based

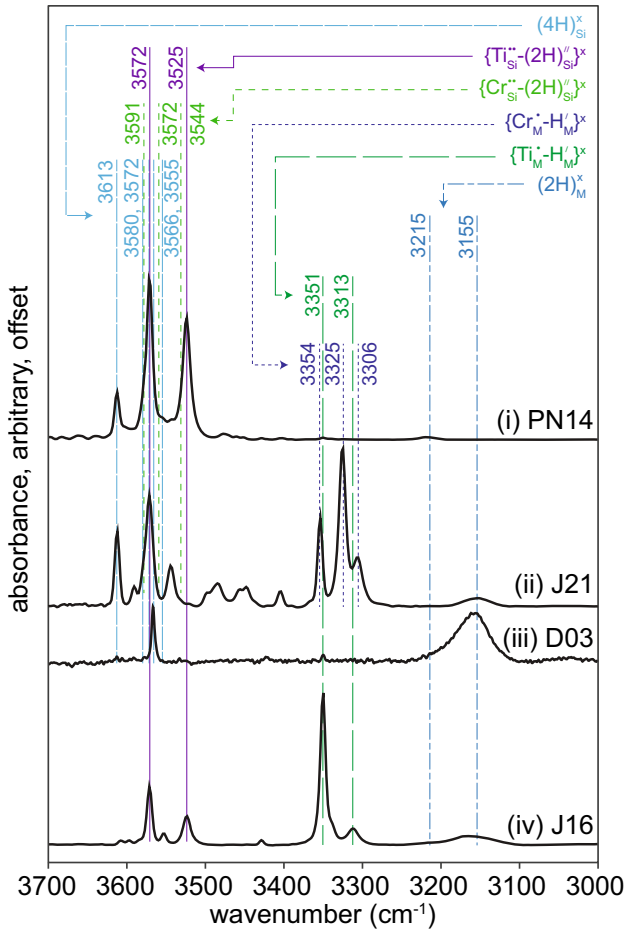

Fig. 1 Example spectra from the four studies being reconsidered, along with the designations of peaks to point defects as described in the text. The absorbance of each spectrum has been scaled and offset arbitrarily, for clarity only. (i) Padrón-Navarta et al. (2014), starting material, mean absorbance ({*E*‖[100] + *E*‖[010] + *E*‖[001]}/3), equivalent to the spectra in their Fig. 2. (ii) Jollands et al. (2021), interface spectrum from experiment HYCRa7. (iii) Demouchy and Mackwell (2003), interface spectrum from experiment Fo2-10, *E*‖[001]. (iv) Jollands et al. (2016a, b), interface spectrum from experiment Hydrol10. Experimental details are provided in Table 2. A version of the same figure without labels and with spectra normalised to 1 cm thickness is provided in the Supplementary Online Material (Fig. S1)

on Berry et al. 2005), then H-out experiments were run in air at 800–1200 °C. The starting materials contained 590 ± 20 wt ppm Ti, with main bands at 3572, 3525 cm^{-1} ($\{Ti^{\bullet\bullet}_{M} - (2H)^{\prime\prime}_{Si}\}^{\times}$); 3613, 3580, 3555, 3572, 3566 cm^{-1} ($(4H)^{\times}_{Si}$). They also observed minor bands at 3220 cm^{-1} ($(2H)^{\times}_{M}$) and 3350 cm^{-1} (potentially $\{Al^{\bullet}_{M} - H^{\prime}_{M}\}^{\times}$ or $\{Fe^{\bullet}_{M} - H^{\prime}_{M}\}^{\times}$). Diffusion coefficients were determined from defect-specific, bulk water concentration (i.e., whole crystal, not spatially resolved) as a function of time. The $(2H)^{\times}_{M}$ defect fell below detectability most rapidly, followed by $\{Ti^{\bullet\bullet}_{M} - (2H)^{\prime\prime}_{Si}\}^{\times}$, then $(4H)^{\times}_{Si}$. The extracted $\{Ti^{\bullet\bullet}_{M} - (2H)^{\prime\prime}_{Si}\}^{\times}$ diffusivities were approximately 0.5–1 order of magnitude lower than those of $(2H)^{\times}_{M}$, but still considerably higher (2–3 orders of magnitude) than the $(4H)^{\times}_{Si}$ diffusivities.

To summarise, the H-in experiments (Demouchy and Mackwell 2003; Jollands et al. 2016b, 2021) show a wide variety of defects along with $(2H)^{\times}_{M}$. Along with $(2H)^{\times}_{M}$, the H-out diffusion experiments (Padrón-Navarta et al. 2014) show mobility of other defects. Taken together, these observations cannot be described by simple diffusion where $(2H)^{\times}_{M}$ exchanges with $Mg^{\times}_{M}$.

Absorption coefficients

Whilst FTIR spectroscopy is a powerful tool for distinguishing different defects, a drawback is that FTIR spectra do not provide absolute water concentrations. Rather, these have to be calculated by means of the Beer–Lambert law which relates concentration to integrated absorbance, using the sample thickness, density and a pre-calibrated absorption coefficient, designated as ε, normally presented with units of L mol^{-1} cm^{-2}, which converts the measured integrated total absorbance into wt. ppm H_2O. There exist several calibrations of the absorption coefficient routinely applied for olivine (Bell et al. 2003; Blanchard et al. 2017; Kovács et al. 2010; Libowitzky and Rossman 1997; Withers et al. 2012), thus for completeness, we apply all of them. The relationships are presented the Supplementary Online Material (Table S1). Jollands et al. (2021) suggested that the Blanchard et al. (2017) and Libowitzky and Rossman (1997) calibrations gave permissible results for their data, as did the Libowitzky and Rossman (1997) calibration pinned to the Bell et al. (2003) calibration at 3550 cm^{-1} and to the Withers et al. (2012) calibration at 3600 cm^{-1}. The latter two were determined simply by maintaining the slope of the Libowitzky and Rossman (1997) calibration in wavenumber-ε space, but adjusting the intercept. However, they also showed that all of these 'permissible' absorption coefficients appeared to underestimate the $\{Cr^{\bullet}_{M} - H^{\prime}_{M}\}^{\times}$ concentration, thus, apparently, none of the absorption coefficients published to date is universally appropriate.

Methodological developments

Spectroscopy-based considerations of defect equilibria

The depth of the previous discussion is only possible given the considerable power of FTIR spectroscopy, which is not only fast, low cost and non-destructive, but also allows simultaneous quantification of both the 'water' concentration (the concentration of O–H bonds over the optical path length) and qualification of the local environment of the O–H bonds, i.e., the point defect to which they can be

Table 2 Experimental conditions used in previous studies, for the samples whose data are reprocessed

Experiment ID	Dopant	T (°C)	P (GPa)	t (h)	$aSiO_2$ buffer	fO_2 buffer	~aH_2O
Demouchy and Mackwell (2003)							
Fo2-5	None	1060	0.2	8	Fo-ens	Ni–NiO	1
Fo2-10	None	1110	0.2	3	Fo-ens	Ni–NiO	1
Jollands et al. (2016a, b)							
Hydrol8	Ti^{3+}, Ti^{4+}	650	1.5	360	Fo-ens	Re–ReO_2	1
Hydrol1	Ti^{3+}, Ti^{4+}	850	1.5	6	Fo-ens	Re–ReO_2	1
Hydrol10	Ti^{3+}, Ti^{4+}	1000	1.5	1	Fo-ens	Re–ReO_2	1
Jollands et al. (2021)							
HYCRa11	Cr^{3+}, Cr^{4+}	750	1.5	125	Fo-ens	Ni–NiO	1
HYCRb5	Cr^{3+}, Cr^{4+}	850	1.5	24	Fo-ens	Ni–NiO	1
HYCRa7	Cr^{3+}, Cr^{4+}	1000	1.5	1.5	Fo-ens	Ni–NiO	1
Padrón-Navarta et al. (2014)							
	Ti^{4+}	800	10^{-4} (1 atm)	0–1304	None	None (air)	0
	Ti^{4+}	900	10^{-4} (1 atm)	0–432	None	None (air)	0
	Ti^{4+}	1000	10^{-4} (1 atm)	0–296	None	None (air)	0

The conditions refer to the diffusion anneal, not any pre-anneal or synthesis step. 'Fo-ens' means the $aSiO_2$ is buffered by the presence of forsterite + enstatite. The activities of H_2O are approximate, assuming pure water in high pressure experiments and a nominally dry atmosphere in air. Padrón-Navarta et al. (2014) do not provide experiment IDs

ascribed. Such descriptions are currently impossible or extremely challenging, for most other trace elements.

If, as postulated above, the only mobile defect is $(2H)_M^\times$, then, to form other defects, the mobile $(2H)_M^\times$ must interact with a defect or species that is already present in the lattice, at which point its mobility is likely reduced. This is akin to the 'trapping' behaviour described for H diffusion in metals (e.g., Causey et al. 2012; Oriani 1970) and the models presented herein represent an extension of such models to H in olivine. We do not use the 'trapping' term as it could be misconstrued to imply irreversible reactions. Such behaviour has been suggested before in the H-in-olivine system, by workers including Ferriss et al. (2018); Jollands et al. (2016a, b, 2019, 2021); Padrón-Navarta et al. (2014) and Thoraval et al. (2019). Note that $(2H)_M^\times$ is the only OH-bearing defect common between the four experimental studies in pure forsterite being considered here (Demouchy and Mackwell 2003; Jollands et al. 2016a, b, 2021; Padrón-Navarta et al. 2014).

Perhaps the clearest example of this interaction involves the formation of $\{Ti_M^{\bullet\bullet} - (2H)_{Si}''\}^\times$, the so-called 'Ti-clinohumite' point defect, generally described as a peak doublet at 3572 and 3525 cm^{-1} (Berry et al. 2005; 2007a; Faul et al. 2016; Jollands et al. 2016b). The 'Ti-clinohumite' name is somewhat misleading—we emphasise that this refers to a hydrous point defect where Ti^{4+} is octahedrally coordinated such as in Ti-clinohumite, $4Mg_2SiO_4{\cdot}Mg_{1-x}(OH)_{2-2x}Ti_xO_{2x}$, where $x \leq 1$ and most commonly $x = 0.5$ (Robison et al. 1973; López Sánchez-Vizcaíno et al. 2005) and not exsolved lamellae of Ti-clinohumite as an individual phase.

This defect was formed in the Jollands et al. (2016b) H-in diffusion experiments, and was apparently mobile in the Padrón-Navarta et al. (2014) H-out diffusion experiments. In the following, we assume that (1) H-free Si vacancies occur in very low concentrations only (Brodholt and Refson 2000; Plushkell and Engell 1968; Smyth and Stocker 1975); (2) Ti^{4+} associated with an M-site vacancy($\{Ti_M^{\bullet\bullet}-V_M''\}^\times$) also has a negligible concentration (Jollands et al. 2016a) and (3) Ti^{4+} replacing Si^{4+} is the most favourable H-free Ti^{4+} substitution mechanism (Berry et al. 2007b; Hermann et al. 2005).

Taken together, in order for $\{Ti_M^{\bullet\bullet} - (2H)_{Si}''\}^\times$ to form in Ti-doped forsterite, if the only mobile species is $(2H)_M^\times$, the most likely reaction is:

$$Ti_{Si}^\times + (2H)_M^\times = \{Ti_M^{\bullet\bullet} - (2H)_{Si}''\}^\times. \quad (1)$$

This describes Ti^{4+} moving from the Si site into an M-site vacancy that was previously associated with the two protons (bonded to O_2 on two SiO_4 tetrahedra; Balan et al. 2011), which then move into coordination with two O^{2-} ions adjacent to the newly-vacant Si site.

Using end-member notation, Eq. (1) is written:

$$Mg_2TiO_4 + MgH_2SiO_4 = MgTiH_2O_4 + Mg_2SiO_4. \quad (2)$$

Whilst every defect and reaction herein can be written in multiple ways as above (see Table 1), we present all in-text reactions only in the form of Kröger–Vink notation used in Eq. (1). All reactions are also presented in end-member notation in the Supplementary Online Material. The reaction described by Eqs. (1) and (2) satisfies the

three assumptions above. This is equivalent to, for example, Eq. (10) of Tollan et al. (2018) and Eq. (15) of Walker et al. (2007).

It is noteworthy that Ferriss et al. (2018) proposed a different reaction where Ti^{4+} is initially octahedrally coordinated, charge balanced by two Fe^{3+} and a silicon vacancy. Notwithstanding the lack of iron in pure forsterite, the $\{Ti_M^{\bullet\bullet} - V_{Si}^{''''} - 2Fe_M^{\bullet}\}^{\times}$ defect is not consistent with the negative $aSiO_2$ versus X_{Ti} relationship from synthesis experiments reported by Hermann et al. (2005). This does not render such a defect impossible, but rather suggests it may be only a minor substitution mechanism for Ti^{4+} in olivine generally.

Likewise, the proposed $\{Cr_M^{\bullet\bullet} - (2H)_{Si}''\}^{\times}$ defect, as observed in the experiments of Jollands et al. (2021), can form by:

$$Cr_{Si}^{\times} + (2H)_M^{\times} = \{Cr_M^{\bullet\bullet} - (2H)_{Si}''\}^{\times}. \quad (3)$$

In both cases, the formation of the H-bearing defect is accompanied by the physical movement of a tetravalent cation from a Si site to a M site.

Jollands et al. (2016b) and Jollands et al. (2021) both observed formation of defects associated with trivalent cations, $\{Cr_M^{\bullet} - H_M'\}^{\times}$ and $\{Ti_M^{\bullet} - H_M'\}^{\times}$. If one makes the assumption that such ions as Cr^{3+} and Ti^{3+}, in their H-free configurations, primarily occupy M sites charge balanced by an M vacancy, e.g., $\{2Cr_M^{\bullet} - V_M''\}^{\times}$ (Burnham and O'Neill 2020; Colson et al. 1989; Evans et al. 2008; Grant and Wood 2010; Jollands et al. 2016a, 2018; Li et al. 1995; Nielsen et al. 1992), then the reactions forming the defects are:

$$\{2Cr_M^{\bullet} - V_M''\}^{\times} + (2H)_M^{\times} = 2\{Cr_M^{\bullet} - H_M'\}^{\times}, \quad (4)$$

and

$$\{2Ti_M^{\bullet} - V_M''\}^{\times} + (2H)_M^{\times} = 2\{Ti_M^{\bullet} - H_M'\}^{\times}. \quad (5)$$

These are equivalent to Eq. (6) of Tollan et al. (2018).

To form $(4H)_{Si}^{\times}$ defects, as were observed by Demouchy and Mackwell (2003) and Jollands et al. (2021), we could invoke Al:

$$\{Al_M^{\bullet} - Al_{Si}'\}^{\times} + 2(2H)_M^{\times} = \{2Al_M^{\bullet} - V_M''\}^{\times} + (4H)_{Si}^{\times}. \quad (6)$$

This is plausible as Al^{3+} in as-grown forsterite is likely mainly in a Tschermak-type configuration, i.e., $\{Al_M^{\bullet} - Al_{Si}'\}^{\times}$ (Coogan et al. 2014; McCarty and Stebbins 2017; Wan et al. 2008). Alternatively, it is also conceivable that a reaction could occur in the pure Mg–Si–O system, e.g.:

$$2(2H)_M^{\times} + Si_{Si}^{\times} = (4H)_{Si}^{\times} + \{Si_i^{\bullet\bullet\bullet\bullet} - 2V_M''\}^{\times}, \quad (7)$$

$$2(2H)_M^{\times} + \{2Mg_i^{\bullet\bullet} - V_{Si}^{''''}\}^{\times} = (4H)_{Si}^{\times} + 2Mg_M^{\times}, \quad (8)$$

or

$$2(2H)_M^{\times} + \{V_{Si}^{''''} - 2V_O^{\bullet\bullet}\}^{\times} = (4H)_{Si}^{\times} + 2\{V_O^{\bullet\bullet} - V_M''\}. \quad (9)$$

Equation (9) is unlikely, given the very high energy required to form $\{V_{Si}^{''''} - 2V_O^{\bullet\bullet}\}^{\times}$, mostly due to the energy required to form and maintain a vacant Si site (Brodholt and Refson 2000).

Taken together and regardless of which reactions are chosen, we can suggest that all of the point defects in Table 1 and illustrated by the spectra shown in Fig. 1, at least have the potential to form by reactions between $(2H)_M^{\times}$ defects and defects that are already present in the crystal lattice. This offers a qualitative explanation as to why these defects should be present in the H-in diffusion experiments (Demouchy and Mackwell 2003; Jollands et al. 2016b). It may also explain how the $\{Ti_M^{\bullet\bullet} - (2H)_{Si}''\}^{\times}$ defect can be apparently mobile in H-out diffusion experiments—the defect can lose its hydrogen to a pathway associated with higher diffusivity (Padrón-Navarta et al. 2014). Next, a methodology is described that can be used to begin to place quantitative constraints on these inter-site reactions.

Data selection and treatment

The results of several experiments were selected from each previous study to model diffusion–reaction processes, details are given in Table 2.

To treat FTIR spectra from the study of Jollands et al. (2021), data from several profiles across experimental samples were selected, then all FTIR spectra from each profile were resolved into a series of Gaussian peak shapes, which were then integrated. Corrections were made to convert absorbance measured with unpolarised light in the (010) plane to total absorbance based on three resolved, unpolarised spectra acquired in the three principal planes (see their Fig. 1). The peaks were then grouped into defect associations, which were $(2H)_M^{\times}$, $\{Cr_M^{\bullet} - H_M'\}^{\times}$, $\{Cr_M^{\bullet\bullet} - (2H)_{Si}''\}^{\times}$, $(4H)_{Si}^{\times}$ and two other defect types that were not identified. The unpolarised spectra of Jollands et al. (2016b), also acquired on the (010) plane, were treated slightly differently. These show no overlap between bands associated with different defects ($\{Ti_M^{\bullet\bullet} - (2H)_{Si}''\}^{\times}$, $(2H)_M^{\times}$, $\{Ti_M^{\bullet} - H_M'\}^{\times}$), so the wavenumber regions representing the different defects were numerically integrated, then a correction was applied to obtain total absorbance, giving defect-specific total absorbance as a function of distance from the crystal edge. Padrón-Navarta et al. (2014) already provides values of defect-specific total absorbance as a function of time (their Table 2), so these values were used directly. Polarised (E||[001])

spectra from the Demouchy and Mackwell (2003) profiles were reprocessed. These show two band groups ($(4H)^{\times}_{Si}$ and $(2H)^{\times}_{M}$), which were numerically integrated, then corrected to total defect-specific absorbance using values derived from polarised spectra, showing the same defects as in the data set of Jollands et al. (2021). In practical terms, this meant that the integrated absorbance of the $(4H)^{\times}_{Si}$ bands was multiplied by 7.4 and the absorbance of the $(2H)^{\times}_{M}$ band was not corrected. The spectra presented by Demouchy and Mackwell (2003) that were reprocessed do not contain any bands in the ~ 3350 cm^{-1} region generally associated with defects associated with trivalent cations. All integrated absorbance values were normalised to 1 cm thickness.

The modelling requires that hydrogen concentrations can be compared with that of other elements, which means that the absorbance values must be converted to concentrations (this is often unnecessary for simple diffusivity calculations). For internal consistency only, the results presented herein used the Libowitzky and Rossman (1997) calibration pinned to the Withers et al. (2012) calibration. The results from modelling using all calibrations, where possible, are provided in the Supplementary Online Material. The different calibrations are presented in Table S1 in the Supplementary Online Material. For diffusion–reaction modelling, the wt. ppm H_2O values are then converted into concentrations of number of defects per formula unit Mg_2SiO_4; this is described in the Supplementary Online Material.

Diffusion–reaction modelling

In order to model the effects discussed above, we follow the 'two step explicit finite different' approach of Dohmen et al. (2010). Readers are referred to the original paper for details, but, essentially, diffusion is modelled as a series of small time and distance steps (explicit finite difference method, Crank 1975; Smith 1985), with diffusion only associated with the $(2H)^{\times}_{M}$ defect. At each time step, diffusion takes the system out of local equilibrium, then a reaction step returns the system to local equilibrium, with the reaction assumed to happen instantaneously. 'Local' refers to the region of the crystal represented by a single distance step in the explicit finite difference numerical model. The methods used for modelling each data set are slightly different, thus are described separately. In the following, D^* describes the diffusion coefficient associated with diffusion reaction modelling and $\tilde{D}$ (Kohlstedt and Mackwell 1998; Demouchy and Mackwell 2003, 2006) the diffusion coefficient extracted directly from fitting profiles of absorbance versus distance along a profile or as a function of time, to an analytical solution to Fick's second law (see Eqs. A19–A21 in the Supplementary Online Material).

Padrón-Navarta et al. (2014): H-out experiments using Ti-doped forsterite

In these experiments, the $\{Ti^{\bullet\bullet}_{M} - (2H)''_{Si}\}^{\times}$ and $(2H)^{\times}_{M}$ defects showed apparently high mobility. The aim of the modelling is to describe curves, here defect-specific bulk water concentration as a function of time, that develop by combination of diffusion and inter-site reaction. The outputs of the model are the concentrations of each defect, which can then be compared with the data from FTIR spectroscopy.

This relatively simple system, assuming we can neglect the low mobility of $(4H)^{\times}_{Si}$ defects, can be described simply using Eq. (1), from which we have:

$$K = \frac{[\{Ti^{\bullet\bullet}_{M} - (2H)''_{Si}\}^{\times}]}{[Ti^{\times}_{Si}][(2H)^{\times}_{M}]}, \tag{10}$$

where square brackets here represent mole fraction of the relevant endmember, assuming concentration and activity are proportional at low concentrations. The concentrations were calculated for each defect individually, assuming that it was the only defect present in a matrix of pure forsterite, which is potentially reasonable given the very low defect concentrations.

We define two other known parameters (model inputs) that can vary independently of K, which are the initial and boundary total H ($\sum$H) and Ti ($\sum$Ti):

$$\sum \mathrm{H} = 2\left[\{Ti^{\bullet\bullet}_{M} - (2H)''_{Si}\}^{\times}\right] + 2\left[(2H)^{\times}_{M}\right] \tag{11}$$

$$\sum \mathrm{Ti} = \left[\{Ti^{\bullet\bullet}_{M} - (2H)''_{Si}\}^{\times}\right] + [Ti^{\times}_{Si}]. \tag{12}$$

The method used for determining the defect concentrations from the initial $\sum$H (i.e., $\sum H_{initial}$) and $\sum$H calculated during the model, which varies as a function of time and space, is the same. Rearranging and substituting these equations yields an analytical solution for $\left[\{Ti^{\bullet\bullet}_{M} - (2H)''_{Si}\}^{\times}\right]$ as a function of K, $\sum$H and $\sum$Ti:

$$\left[\{Ti^{\bullet\bullet}_{M} - (2H)''_{Si}\}^{\times}\right] = \left(\frac{1}{4}\left(K\sum \mathrm{H} + 2K\sum \mathrm{Ti} - \left(K^2\left(\sum \mathrm{H}\right)^2 - 4K^2\sum \mathrm{H}\sum \mathrm{Ti} + 4K^2\left(\sum \mathrm{Ti}\right)^2 + 4K\sum \mathrm{H} + 8K\sum \mathrm{Ti} + 4\right)^{1/2} + 2\right)\right)/K. \tag{13}$$

From Eq. (13), the other two unknowns are calculated:

$$\left[(2\mathrm{H})_{\mathrm{M}}^{\times}\right]=\frac{1}{2}\sum \mathrm{H}-\left[\{\mathrm{Ti}_{\mathrm{M}}^{\bullet\bullet}-(2\mathrm{H})_{\mathrm{Si}}^{\prime\prime}\}^{\times}\right], \tag{14}$$

and

$$\left[\mathrm{Ti}_{\mathrm{Si}}^{\times}\right]=\sum \mathrm{Ti}-\left[\{\mathrm{Ti}_{\mathrm{M}}^{\bullet\bullet}-(2\mathrm{H})_{\mathrm{Si}}^{\prime\prime}\}^{\times}\right]. \tag{15}$$

Equations (13)–(15) are firstly used to determine the initial condition of $\mathrm{Ti}_{\mathrm{Si}}^{\times}$, $(2\mathrm{H})_{\mathrm{M}}^{\times}$ and $\{\mathrm{Ti}_{\mathrm{M}}^{\bullet\bullet}-(2\mathrm{H})_{\mathrm{M}}^{\prime\prime}\}^{\times}$, using a fixed $\sum$H and $\sum$Ti of 590 wt. ppm, and an initial guess for K. $\sum$H at the boundary is set to zero. These models assume mass balance, charge balance and site balance. The latter is problematic, especially given that H does not occupy Si or Mg sites, but rather forms OH groups (e.g., see Table 1).

Then, diffusion is modelled using an explicit finite difference approximation of Fick's second law in three dimensions. The model represents a cube, with dimensions 200 × 200 × 200 µm, based on the data of Padrón-Navarta et al. (2014) (~ 100–300 µm, see their Supplementary Online Material A) divided into 10 × 10 × 10 µm voxels, which is a trade-off between accuracy (better with smaller voxels) and computational time (better with larger voxels). The effect of voxel size on model outputs is discussed below. We assume that diffusion is anisotropic, with $\log_{10}D^{*}_{[001]}=\log_{10}D^{*}_{[010]}+0.5=\log_{10}D^{*}_{[100]}+1$, based on Demouchy and Mackwell (2003) and Jollands et al. (2016b). The $\log_{10}D^{*}_{[001]}$ is a model input, from which $\log_{10}D^{*}_{[010]}$ and $\log_{10}D^{*}_{[100]}$ are determined. The model is set up as six cubic matrices, representing the three outputs ($\mathrm{Ti}_{\mathrm{Si}}^{\times}$, $(2\mathrm{H})_{\mathrm{M}}^{\times}$ and $\{\mathrm{Ti}_{\mathrm{M}}^{\bullet\bullet}-(2\mathrm{H})_{\mathrm{Si}}^{\prime\prime}\}^{\times}$) and three inputs ($\sum$H, $\sum$Ti and K). At each time step, diffusion occurs only in the $(2\mathrm{H})_{\mathrm{M}}^{\times}$ matrix. Then, the $\sum$H matrix is recalculated according to Eq. (11). As $\sum$Ti and K are constant (these assumptions are discussed below along with other model caveats), the new values of $\left[\mathrm{Ti}_{\mathrm{Si}}^{\times}\right]$, $\left[(2\mathrm{H})_{\mathrm{M}}^{\times}\right]$ and $\left[\{\mathrm{Ti}_{\mathrm{M}}^{\bullet\bullet}-(2\mathrm{H})_{\mathrm{Si}}^{\prime\prime}\}^{\times}\right]$ can be calculated using Eqs. (13)–(15) for each point in their respective matrices, representing the reaction step where hydrogen is re-distributed. Finally, the mean concentrations of the three defects and $\sum$H are calculated from each matrix, excluding the voxels representing the faces and recorded. Then, another time step begins with diffusion, hydrogen redistribution, and so on, until the total model duration is reached. For this model, the outputs are the mean concentration of each defect as a function of time.

The output vectors were then linearly interpolated to give the concentrations of each defect at the time steps measured by Padrón-Navarta et al. (2014). These values were then incorporated into a solver (lsqnonlin in MATLAB™) and the values of the three model inputs, D^{*}, K and $\sum$H, that best fit the data were determined by non-linear least-squares regression. $\sum$Ti was kept constant according to the EPMA data, assuming its diffusivity is low enough to be negligible (Cherniak and Liang 2014; Jollands et al. 2016a). Attempts were initially made to approximate uncertainties using the constant chi-square boundary method (Press et al. 2007), but this naturally assumes that the model is fully appropriate for describing the data and requires the uncertainty associated with every point along a distance–concentration or time–concentration profile to be constrained. This in turn means that the reduced chi-squared should be close to 1. In general, this is not what we find, without arbitrarily adjusting the uncertainties associated with each point along profiles, which suggests that the model is either not fully appropriate for describing the process (most likely explanation, discussed below with respect to model caveats) or the uncertainties are incorrectly determined. The final result is that uncertainties determined for each fit using a constant chi-square boundary method are probably meaningless and, more likely, misleading. In addition, they are completely subsumed by uncertainties associated with, for example, absorption coefficients and the chemistry of the starting materials. Therefore, for this and all following models, we do not report uncertainties associated with individual fits. This must be considered when assessing the validity of the proposed models.

Jollands et al. (2016b): H-in experiments using Ti-doped forsterite

Following Jollands et al. (2016b), we assume that the only H-bearing defects present were $(2\mathrm{H})_{\mathrm{M}}^{\times}$, trivalent Ti with H, $\{\mathrm{Ti}_{\mathrm{M}}^{\bullet}-\mathrm{H}_{\mathrm{M}}^{\prime}\}^{\times}$ and the 'Ti-clinohumite' type defect, $\{\mathrm{Ti}_{\mathrm{M}}^{\bullet\bullet}-(2\mathrm{H})_{\mathrm{Si}}^{\prime\prime}\}^{\times}$. The relevant reactions are represented by Eqs. (1) and (5). It is important to reiterate that, despite being hardly observed in natural terrestrial systems, these experiments were assumed to contain considerable Ti^{3+}. This was because there was a long, high T, low fO_2 pre-anneal/Ti-doping step prior to the H diffusion anneals, as described above.

From these reactions, we have two Ks, the first of which is the same as Eq. (9), now denoted $K1$. The second, now $K2$, is:

$$K2=\frac{[\{\mathrm{Ti}_{\mathrm{M}}^{\bullet}-\mathrm{H}_{\mathrm{M}}^{\prime}\}^{\times}]^{2}}{[\{2\mathrm{Ti}_{\mathrm{M}}^{\bullet}-V_{\mathrm{M}}^{\prime\prime}\}^{\times}][(2\mathrm{H})_{\mathrm{M}}^{\times}]}. \tag{16}$$

We then define the sums of H, Ti^{3+} and Ti^{4+} as knowns:

$$\sum \mathrm{H}=2\left[\{\mathrm{Ti}_{\mathrm{M}}^{\bullet\bullet}-(2\mathrm{H})_{\mathrm{Si}}^{\prime\prime}\}^{\times}\right]+2\left[(2\mathrm{H})_{\mathrm{M}}^{\times}\right]+\left[\{\mathrm{Ti}_{\mathrm{M}}^{\bullet}-\mathrm{H}_{\mathrm{M}}^{\prime}\}^{\times}\right] \tag{17}$$

$$\sum \mathrm{Ti}^{3+}=\left[\{\mathrm{Ti}_{\mathrm{M}}^{\bullet}-\mathrm{H}_{\mathrm{M}}^{\prime}\}^{\times}\right]+2[\{2\mathrm{Ti}_{\mathrm{M}}^{\bullet}-V_{\mathrm{M}}^{\prime\prime}\}^{\times}] \tag{18}$$

$$\sum \mathrm{Ti}^{4+} = \left[\{\mathrm{Ti}_{\mathrm{M}}^{\bullet\bullet} - (2\mathrm{H})_{\mathrm{Si}}''\}^{\times}\right] + \left[\mathrm{Ti}_{\mathrm{Si}}^{\times}\right] \quad (19)$$

In this case, the Ti concentration cannot be considered as constant along the profiles—the starting material used by Jollands et al. (2016a, b) had a U-shaped Ti profile varying from ~ 260 to ~ 440 wt. ppm. The Ti profile from Jollands et al. (2016a, b) was fitted to an error function form—this was used to define the Ti concentration in the model. Therefore, $\sum$Ti is constant as a function of time, but not space.

These equations cannot be solved analytically. Instead, the concentration of $(2\mathrm{H})_{\mathrm{M}}^{\times}$ is found as the root of a polynomial function. Then, the other four unknowns ($\left[\{\mathrm{Ti}_{\mathrm{M}}^{\bullet} - \mathrm{H}_{\mathrm{M}}'\}^{\times}\right]$, $[\{2\mathrm{Ti}_{\mathrm{M}}^{\bullet} - V_{\mathrm{M}}''\}^{\times}]$, $[\mathrm{Ti}_{\mathrm{Si}}^{\times}]$, $\left[\{\mathrm{Ti}_{\mathrm{M}}^{\bullet\bullet} - (2\mathrm{H})_{\mathrm{Si}}''\}^{\times}\right]$), are calculated from $[(2\mathrm{H})_{\mathrm{M}}^{\times}]$. The relevant equations are given in the Supplementary Online Material.

The roots of the polynomial were found using the *fzero* command on MATLAB™. Whilst the system has at least two roots with any combination of input values, only one yields positive concentrations for all defects. This true root was found using ad hoc starting guesses, finding the associated root and thus the concentration of $(2\mathrm{H})_{\mathrm{M}}^{\times}$, calculating the concentration of the other four types of point defect, then repeating with different random starting guesses until the concentrations of all five types of point defect were positive. An example of the function is shown in the Supplementary Online Material (Fig. S2), where two positive $(2\mathrm{H})_{\mathrm{M}}^{\times}$ defects give $f = 0$, but only one gives positive concentrations of all defects. With the reaction defined, the system was modelled using a 1D explicit finite difference method, with Δx of 10 µm. As before, the results of a diffusion step were calculated, then the concentrations of each defect were recalculated according to the above relationships. In order to expedite modelling, the stable roots were determined for a series of different values of $K1$, $K2$, $\sum$H, $\sum \mathrm{Ti}^{4+}$, which were placed into three 4-D lookup tables (one for each $\sum \mathrm{Ti}^{4+}/\sum$Ti value, see below), each with ~ 4×10^7 points. Then, during modelling, the values of $(2\mathrm{H})_{\mathrm{M}}^{\times}$ and thus the other four defects, were found using linear interpolation (MATLAB™ function *interpn*) within this lookup table. Unlike the previous section, the model outputs are the concentration of each defect as a function of distance, which were matched to the data using nonlinear least squares regression, to yield the values of $K1$, $K2$, $\sum$H (boundary) and D^*. Because there was some uncertainty regarding $\sum \mathrm{Ti}^{4+}/\sum$Ti in Jollands et al. (2016a, b), models were run using $\sum \mathrm{Ti}^{4+}/\sum$Ti of 0.1, 0.25 and 0.4. The results presented herein used $\sum \mathrm{Ti}^{4+}/\sum$Ti of 0.1—others are presented in the Supplementary Online Material for comparison only and not discussed further. This was only performed for the experiments from the main series of Jollands et al. (2016b), i.e., their Re–ReO_2, enstatite buffered experiments at 1.5 GPa.

Jollands et al. (2021): H-in experiments using Cr-doped forsterite

These experiments yielded extremely complex FTIR spectra, including many bands that could not be assigned definitively to known point defects. These complexities mean that we cannot provide a fully satisfactory description of all reactions, therefore we choose to just model the two main OH-bearing point defects and their two dry equivalents ($\{\mathrm{Cr}_{\mathrm{M}}^{\bullet} - \mathrm{H}_{\mathrm{M}}'\}^{\times}$, $\{2\mathrm{Cr}_{\mathrm{M}}^{\bullet} - V_{\mathrm{M}}''\}^{\times}$, $\mathrm{Cr}_{\mathrm{Si}}^{\times}$, $\{\mathrm{Cr}_{\mathrm{M}}^{\bullet\bullet} - (2\mathrm{H})_{\mathrm{Si}}''\}^{\times}$) as well as the mobile defect $(2\mathrm{H})_{\mathrm{M}}^{\times}$. This represents between 80 and 90% of the total absorbance of the experimental spectra.

With these simplifications, the system is described by Eqs. (3) and (4). Therefore, the equations defining the system are the same as Eqs. (16)–(19), except with Cr replacing Ti. The modelling was completed in approximately the same way as for the Ti experiments, with the only substantial difference being the definition of the Cr oxidation state in the starting material. We assume a constant amount of Cr and assign $\mathrm{Cr}^{3+}/\sum\mathrm{Cr} = 0.7$ as determined by Jollands et al. (2021) (see their Sect. 4.3), meaning that the lookup table had only three dimensions. This was calculated for experiments from the main series of Jollands et al. (2021), i.e., Ni–NiO, enstatite buffered experiments at 1.5 GPa. According to the XANES data reported by Jollands et al. (2021), the assumption that $\mathrm{Cr}^{3+}/\sum\mathrm{Cr}$ is constant is not valid only within a few tens of µms of the crystal rim, but the relatively poor spatial resolution of FTIR data conveniently means that this is not problematic for the modelling in this study.

H diffusion in pure forsterite (Demouchy and Mackwell 2003)

Two profiles from the dataset of Demouchy and Mackwell (2003) were re-evaluated. We consider only the experiments where the only defects present in the FTIR spectra are consistent with a pure Mg–Si–O–H system, i.e., no trace elements—their 'Fo2' series. Ironically, it is these experiments in the simplest system that are the most challenging to model, because the defect population in the starting material is not explicitly set by trace element doping, but will likely be inherited from the conditions of synthetic growth, so is poorly constrained. The profiles of Demouchy and Mackwell (2003) show simple spectra with only $(2\mathrm{H})_{\mathrm{M}}^{\times}$ and $(4\mathrm{H})_{\mathrm{Si}}^{\times}$ defects, showing similar diffusive length scales.

We model only Eq. (7), which is likely incorrect, thus is used here as a proof of concept only, i.e., to demonstrate that $(4\mathrm{H})_{\mathrm{Si}}^{\times}$ could form from $(2\mathrm{H})_{\mathrm{M}}^{\times}$ and some pre-existing point defect. For this reason, only two profiles are modelled (profiles parallel to [001] from their experiments Fo 2_5 and Fo 2_10).

In Eq. (7), it is reasonable to assume that the activity of $\mathrm{Si}_{\mathrm{Si}}^{\times}$ is 1 or at least constant, thus K for the reaction is:

$$K = \frac{\left[(4H)^{\times}_{Si}\right]\left[\{Si^{\bullet\bullet\bullet\bullet}_{i} - 2V''_{M}\}^{\times}\right]}{\left[(2H)^{\times}_{M}\right]^{2}}. \quad (20)$$

In order to simplify modelling, an arbitrary assumption is made that $\left[(4H)^{\times}_{Si}\right]$ and $[\{ Si^{\bullet\bullet\bullet\bullet}_{i} - 2V''_{M}\}^{\times}]$ are equal, if this is the only reaction capable of forming either defect. Again, this assumption is certainly too simple, but considerably simplify the calculations.

$$K = \frac{\left[(4H)^{\times}_{Si}\right]^{2}}{\left[(2H)^{\times}_{M}\right]^{2}}. \quad (21)$$

With only two unknowns, we require one more constrained variable, the obvious choice is $\sum H$:

$$\sum H = 2\left[(2H)^{\times}_{M}\right] + 4\left[(4H)^{\times}_{Si}\right]. \quad (22)$$

For this system, there exists an analytical solution:

$$\left[(2H)^{\times}_{M}\right] = \frac{\frac{1}{2}\sum H}{2K^{1/2}+1}, \quad (23)$$

from which $\left[(4H)^{\times}_{Si}\right]$ is determined:

$$\left[(4H)^{\times}_{Si}\right] = \frac{\sum H}{4} - \frac{\left[(2H)^{\times}_{M}\right]}{2}. \quad (24)$$

The system is then modelled using the same diffusion–reaction method as for the other in-diffusion experiments.

An important point here and model caveat, is that we consider the reaction forming $(4H)^{\times}_{Si}$ and $\{Si^{\bullet\bullet\bullet\bullet}_{i} - 2V''_{M}\}^{\times}$ from $(2H)^{\times}_{M}$ and $Si^{\times}_{Si}$ in isolation, i.e., we effectively assume that this is the only reaction occurring in the crystal. This a simplification—it may also be necessary to consider, at least, the formations of Mg- and Si-Frenkel defects:

$$Mg^{\times}_{M} = Mg^{\bullet\bullet}_{i} + V''_{M} \quad (25)$$

$$Si^{\times}_{Si} = Si^{\bullet\bullet\bullet\bullet}_{i} + V''''_{Si}. \quad (26)$$

However, according to thermodynamic modelling (Muir et al. 2022), the concentration of extrinsic H-bearing defects is predicted to be several orders of magnitude higher than the concentration of intrinsic defects. Therefore, at least according to this modelling, the effect of intrinsic defects on the dynamics of extrinsic defect reactions is vanishingly small.

Defect calculations using density functional theory

To complement the diffusion–reaction modelling, the net energetics of the four main reactions were calculated by density functional theory (DFT), i.e., forming $\{Ti^{\bullet\bullet}_{M} - (2H)''_{Si}\}^{\times}$, $\{Cr^{\bullet\bullet}_{M} - (2H)''_{Si}\}^{\times}$, $\{Cr^{\bullet}_{M} - H'_{M}\}^{\times}$ and $\{Ti^{\bullet}_{M} - H'_{M}\}^{\times}$ (Eqs. (1), (3), (4) and (5) respectively). The motivation for using DFT in this study is not to provide an exact and rigourous simulation of all defect energies, but to explore the validity of diffusion–reaction models using a fully independent method. Extensive documentation of the same DFT method as employed in this study is presented in Muir et al. (2022), which also considers OH-bearing defects in olivine. The following is a brief description of the method—readers are referred to Muir et al. (2022) and the Supplementary Online Material for further information.

The concentrations of H, Ti and Cr used for the modelling, for the different datasets were, in wt. ppm: Jollands et al. (2016a, b): H_2O: 20–30, Ti^{4+}: 30, Ti^{3+}: 300; Padrón-Navarta et al. (2014): H_2O: 100, Ti^{4+}: 600; Jollands et al. (2021): H_2O: 15, Cr^{3+}: 110, Cr^{4+}: 50. These are approximations based on the concentrations extracted from reprocessing the data, as described above. Differences between these values and published values mainly relate to different absorption coefficients used to extract H_2O contents.

All calculations were done using planewave density functional theory (DFT), using version 16.11 of the CASTEP code (Clark et al. 2005). On-the-fly ultra-soft pseudopotentials were used with 2*s*/3*p* and 3*s*/2*s*/2*p*, 3*s*/3*p*, 1*s*, 3*p*/3*s*/3*d*/4*s* and 3*s*/3*p*/3*d*/4*s* electrons in the valence band for Mg, O, Si, H, Ti and Cr, respectively. The Perdew–Burke–Ernzerhof (Perdew et al. 1996) exchange–correlation functional (a revised generalised gradient approximation functional) was used. In the calculations, pairs/trios inside curly braces are placed in a nearest neighbour positions to prevent the development of charged dipoles.

Energy calculations were done at 0, 5 and 10 GPa and at 1000, 1500 and 2000 K. The energy at the pressure and temperature of interest was determined from polynomial fits to these calculated values (pressure first, then temperature). Pressures were corrected using a linear fit of calculated volumes to experimental volumes, with equations and values given in Muir et al. (2022). Calculations were done using (2 × 1 × 2) (single site defects) or (4 × 2 × 4) forsterite supercells (multisite defects) alongside a planewave cutoff of 1000 eV (96,485 kJ mol^{-1}) with a (2 × 2 × 2) Monkhorst–Pack k-point grid (Monkhorst and Pack, 1976). In each case, the energy cost/gain of placing a defect in a cell was calculated. As the concentration of defects is very small, we assume that across the concentration range of interest they have ideal behaviour, i.e., that their non-configurational entropy is a linear function of concentration and that defect−defect interactions are negligible. To test this, a $\{Ti^{\bullet\bullet}_{M} - (2H)''_{Si}\}^{\times}$ and a $\{Cr^{\bullet}_{M} - H'_{M}\}^{\times}$ were placed into both a (2 × 1 × 2) and a (4 × 2 × 4) supercell and the energy of placing a defect varied by < 3 meV/defect, showing strong ideality. The calculations should ideally determine the energy of adding a defect at the dilute limit, which is

the limit at which placing a defect does not vary the size of the unit cell of forsterite. To approximate this limit, the unit cell was frozen to the dimensions of the forsterite unit cell at the appropriate temperature and pressure in all calculations. Runs containing Cr were spin-polarised and Cr was simulated in the high and low spin state. The high spin state was always the most stable, both enthalpically and energetically.

To calculate the energetics of the reactions, our method was as follows. Firstly, the arrangement of each defect with the lowest enthalpy was determined. For each defect, all possible arrangements of the defect were tested which includes (1) different possible arrangements of the hydrogen atoms; (2) placement on different sites in the crystal (Mg-centered defects can exist at M1 or M2 sites) and (3) the geometric arrangement of the pair/trio, whilst maintaining next neighbour proximity. For hydrogen arrangements, each hydrogen atom is bound to a specific O site on the edge of the vacancy and with the hydrogen pointing either inside or outside the vacancy. Given the large number of possible arrangements (e.g., 90 arrangements for $\{Ti_M^{\bullet\bullet} - (2H)_{Si}''\}^{\times}$), the arrangements and their relative enthalpies are presented in the Supplementary Online Material.

To simplify calculations, the enthalpies of different $\{Ti_M^{\bullet\bullet} - (2H)_{Si}''\}^{\times}$, $\{Cr_M^{\bullet} - H_M'\}^{\times}$ and $\{2Cr_M^{\bullet} - V_M''\}^{\times}$ configurations, already calculated by Muir et al. (2022), were used as starting points to determine the lowest energy arrangements of $\{Cr_M^{\bullet\bullet} - (2H)_{Si}''\}^{\times}$, $\{Ti_M^{\bullet} - H_M'\}^{\times}$ and $\{2Ti_M^{\bullet} - V_M''\}^{\times}$, respectively. Specifically, to determine the lowest energy arrangement of $\{Cr_M^{\bullet\bullet} - (2H)_{Si}''\}^{\times}$, Ti^{4+} was replaced with Cr^{4+} in every $\{Ti_M^{\bullet\bullet} - (2H)_{Si}''\}^{\times}$ arrangement with relative enthalpy < 0.5 eV at 0 GPa. This means that the relative enthalpy of $\{Cr_M^{\bullet\bullet} - (2H)_{Si}''\}^{\times}$ was determined for 28 configurations, rather than the 270 configurations determined for $\{Ti_M^{\bullet\bullet} - (2H)_{Si}''\}^{\times}$ (see the Supplementary Online Material). Similarly, Cr^{3+} was replaced by Ti^{3+} in $\{Cr_M^{\bullet} - H_M'\}^{\times}$ defects with the same 0.5 eV cutoff, meaning the energies of 78 rather than 108 configurations were determined for $\{Ti_M^{\bullet} - H_M'\}^{\times}$.

Secondly, the high temperature free energies for each defect were determined. To achieve this, the phonons of the most stable arrangements of each type of point defect were calculated using linear displacements (displacements of 0.01 bohr) in the CASTEP code (http://www.castep.org). This was done for at least five different volumes for each system, with the energy calculated as a function of volume (including thermal expansion) using Quasi-harmonic approximation (QHA) calculations. The phonons were only calculated at the gamma point given limitations of linear displacement calculations. There are two major assumptions here, (1) that the energy of the defects can be adequately represented by harmonic oscillations and (2) that the most stable arrangements of the defects under static conditions (where the most stable arrangements are determined) are also the most stable under high temperature conditions. This assumption was tested by explicitly calculating the high temperature (1000–2000 K) energies of some arrangements of $\{Cr_M^{\bullet} - H_M'\}^{\times}$. The energy variations at high temperatures are small enough to be negligible in the reaction calculations—results of the test are presented in the Supplementary Online Material. The QHA equations are reported in Muir et al. (2022), along with a discussion on the limitations with regards to this method.

Finally, the equilibrium position of each reaction was determined by minimising the free energy. For any arbitrary progression (x) of the reaction, the free energy is defined as two terms—the first being the non-configurational term which is $x\Delta G$, where ΔG is determined from the energies of the defects and the second being the configurational term. This configurational term is complex but is determined in two steps (with equations and discussion presented in Muir et al. 2022). First, for each defect that is present, the probability of each of its arrangements occurring is calculated based on its relative enthalpy. The overall configurational entropy is then determined using the Gibbs configurational entropy formula and the Stirling approximation. Then, the value of x that gives the minimum free energy is determined. We assume that the relative energy of different arrangements of defects is similar to the relative enthalpy. The results of a test of this assumption for one defect $\{Cr_M^{\bullet} - H_M'\}^{\times}$ is provided in the Supplementary Online Material. In general, this is a very minor term and small variations in the phonon frequencies of different arrangements of the same type of defect causes little modification to the overall energies and distributions of hydrogen. This is because these terms define the internal configurational entropy of defects which have a number of possible arrangements (W) on the order of ~ 100 or less. Entropy relies upon the logarithm of arrangements ($\ln W$) so this term is always small when compared with the number of possible arrangements of defects that have concentration on the order of parts-per-million across different cationic sites in the crystal which is many orders of magnitude larger. The more problematic part of this assumption is the possibilty that one arrangement has high enthalpy, but is the most stable arrangement at high temperature. In this case, the energy of the reactions could be incorrectly determined which could lead to substantial changes in reaction products. The high temperature parts of different arrangements are similar, as variations in the position of the hydrogen or the defect cations only makes small modifications to overall phonon frequencies.

Benchmarking our calculations against previous experiments is challenging due to the considerable experimental difficulty in measuring defect concentrations and their energies. More reliable tests are against properties that depend upon defect concentrations, such as diffusion. Using the

same modelling scheme and the same set of assumptions as in this work, calculations have been benchmarked using experimental diffusion rates of Mg in both anhydrous and hydrous forsterite (Muir et al. 2020, 2021a). These methods have already been used to estimate hydrogen diffusivity (Muir et al. 2021b) and a similar diffusivities to those determined in this study were obtained.

Results

Diffusion–reaction models: effects of the input parameters on output profiles

In this section, we consider how changing the various input parameters, K, D^*, initial and boundary conditions, changes the model outputs. This is done, for brevity, for a system based on the Padrón-Navarta et al. (2014) system only, using just Eq. (10) for the reaction, i.e., the simple reaction forming $\{Ti_M^{\bullet\bullet} - (2H)_{Si}''\}^\times$ from $Ti_{Si}^\times$ and $(2H)_M^\times$. For illustration purposes, the model was reformatted into one dimension, plane−sheet geometry, considering a 2 mm long profile parallel to [001], with boundaries with a constant composition at each end. Models were run both assuming both H-out (as in the experiments) and H-in. Exact model parameters are given in the figure captions.

Reaction constant, *K*

Examples of models run with changing K, but all other parameters constant, are shown in Fig. 2. The forward reaction (Eq. (1)) produces $\{Ti_M^{\bullet\bullet} - (2H)_{Si}''\}^\times$ from $Ti_{Si}^\times$ and $(2H)_M^\times$. Therefore, a high K (10^6 in Fig. 2) means a relatively higher concentration of the $\{Ti_M^{\bullet\bullet} - (2H)_{Si}''\}^\times$ defect. In a H-out experiment, this means that H is retained, because most of the H remains coupled to Ti^{4+} and does not move into its mobile configuration (i.e., $(2H)_M^\times$). This leads to short profiles, with a high core concentration. If K is lower (10^4 in Fig. 2), then $Ti_{Si}^\times$ and $(2H)_M^\times$ are favoured. This means that at time $t=0$ (initial model set up), much of the $\{Ti_M^{\bullet\bullet} - (2H)_{Si}''\}^\times$ will already decompose into $Ti_{Si}^\times$ and $(2H)_M^\times$, giving a lower core $\{Ti_M^{\bullet\bullet} - (2H)_{Si}''\}^\times$ concentration and as more of the hydrogen is in its mobile configuration, H loss will be rapid.

In an H-in experiment, a relatively high K means that most mobile $(2H)_M^\times$ defects will be consumed forming immobile $\{Ti_M^{\bullet\bullet} - (2H)_{Si}''\}^\times$ defects. This effectively prevents $(2H)_M^\times$ from moving rapidly through the crystal, leading to short $\{Ti_M^{\bullet\bullet} - (2H)_{Si}''\}^\times$ profiles with high concentrations and almost no discernible $(2H)_M^\times$ profile. Where K is relatively lower, only a small number of $(2H)_M^\times$ defects are consumed to form $\{Ti_M^{\bullet\bullet} - (2H)_{Si}''\}^\times$, thus we would predict the formation of long $(2H)_M^\times$ profiles with relatively high concentrations and long $\{Ti_M^{\bullet\bullet} - (2H)_{Si}''\}^\times$ profiles with relatively low concentrations (both described relative to the higher K case).

It is important to note that the use of the terms 'high' and 'low' to describe K of 10^6 and 10^4, respectively, are relative indications only. The overall behaviour is also affected by D^* and the concentrations of H and Ti, thus the reader should keep in mind that similar behaviour could be observed with very different Ks, if the other parameters are adjusted appropriately.

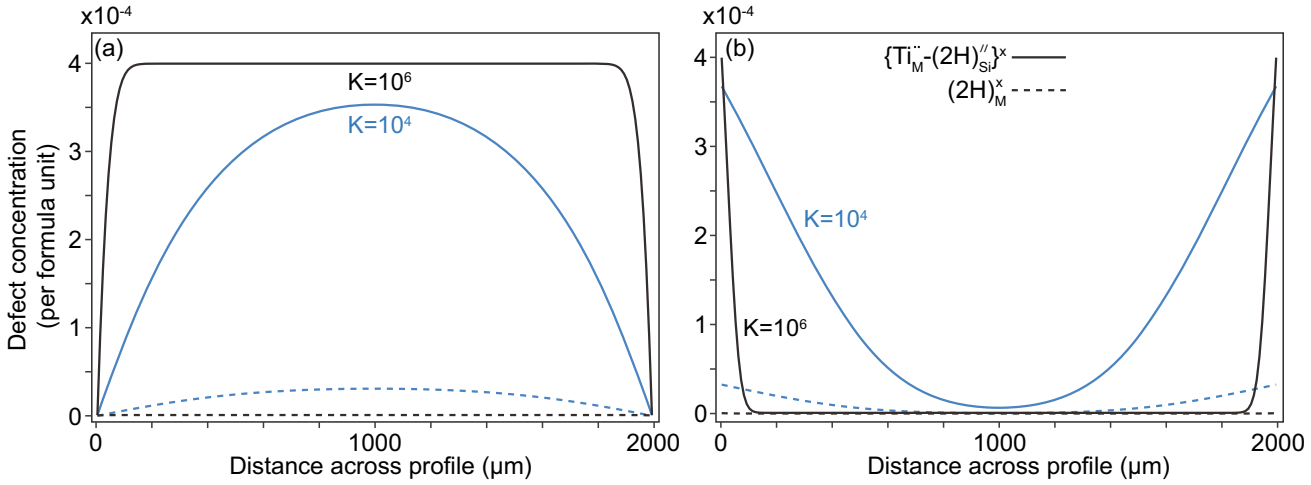

Fig. 2 The effect of K on defect-specific profiles, where all other parameters are constant. Higher K yields shorter profiles for the $\{Ti_M^{\bullet\bullet} - (2H)_{Si}''\}^\times$ defect. Concentrations are per formula unit. **a** K: 10^4 (blue) or 10^6 (black), Ti (initial and boundary): 1.5×10^{-3}, H (initial): 8×10^{-4}, H (boundary): 1.5×10^{-6}, time: 100,000 s (~28 h); dx: 10 μm, D^*: 10^{-11} m^2s^{-1} (approximately equivalent to D^* at 900 °C). **b** As **a**, except H (boundary): 8×10^{-4} and H (initial): 1.5×10^{-6}

Ti and H concentrations

As the Ti concentration decreases, keeping all other variables constant, the profile lengths associated with $\{Ti_M^{\bullet\bullet} - (2H)_{Si}''\}^{\times}$ increase. This is because the relative concentration of $(2H)_M^{\times}$ to $\{Ti_M^{\bullet\bullet} - (2H)_{Si}''\}^{\times}$ increases with lower $\sum$Ti, thus a larger proportion of hydrogen is mobile. Changing the H concentration has very little effect on the profile lengths and geometry, as long as the amount of H is not sufficiently greater than the Ti concentration. Examples are presented in Fig. 3.

Diffusion coefficient (D^*)

Increasing the diffusion coefficient (D^*) in the diffusion–reaction model has a similar effect to increasing $\tilde{D}$ in a simple diffusion model, i.e., a one order of magnitude D^* increase leads to ~ $10^{0.5}$ × longer profiles. An example of output profiles where D^* is changed, but all other parameters are kept constant, is shown in Fig. 4a. Also shown are the outputs of profiles where both the input D^*s and Ks were changed, were fitted to an analytical solution to Fick's second law (eq. A19 in the Supplementary Online Material), to give output $\tilde{D}$s. This was done > 500 times for different input combinations, with the results contoured in Fig. 4b. Increasing either the input D^* or K by one order of magnitude has broadly the same effect on the output $\tilde{D}$.

Convergence

The applied Δx (and Δy, Δz for the 3D case) values were chosen as a compromise between computational time (lower with coarser grid) and accuracy (higher with finer grid). The following considers the possible degree of inaccuracy associated with the relatively coarse grid used in the models.

Two models were run with the same input parameters (D^*, K, concentrations), but different Δx (0.1–100 µm for 1D, 1–50 µm for 3D). The model outputs are presented in the Supplementary Online Material (Fig. S3) along with model parameters. In each case, the model with the smallest grid size was taken as a "reference" and all other models were compared with those to assess inaccuracy. The discrepancy was quantified in two ways. First, an approximate % discrepancy between the reference model and the "test" model with a higher Δx was calculated, as the root mean squared difference between the model outputs (defect-specific H vs. distance or time), divided by the mean of the "test" model, multiplied by 100. Second, the outputs of both models were fitted to an analytical solution of Fick's second law to estimate a phenomological $\tilde{D}$ and an interface or initial concentration.

In the 1D case, the % discrepancy between models with $\Delta x = 0.1$ µm and $\Delta x = 10$ µm is ~ 1% only (Fig. S3a–c). In the 3D case, the % discrepancy between the models with $\Delta x = \Delta y = \Delta z$ of 10 µm and 1 µm is greater, around 7% (Fig. S3 d–f). In both cases, however, the extracted $\tilde{D}$ s determined using the coarse grid are within 0.05 log units of the same determined using the smallest Δx. This effectively means that the length scales of the profiles or the forms

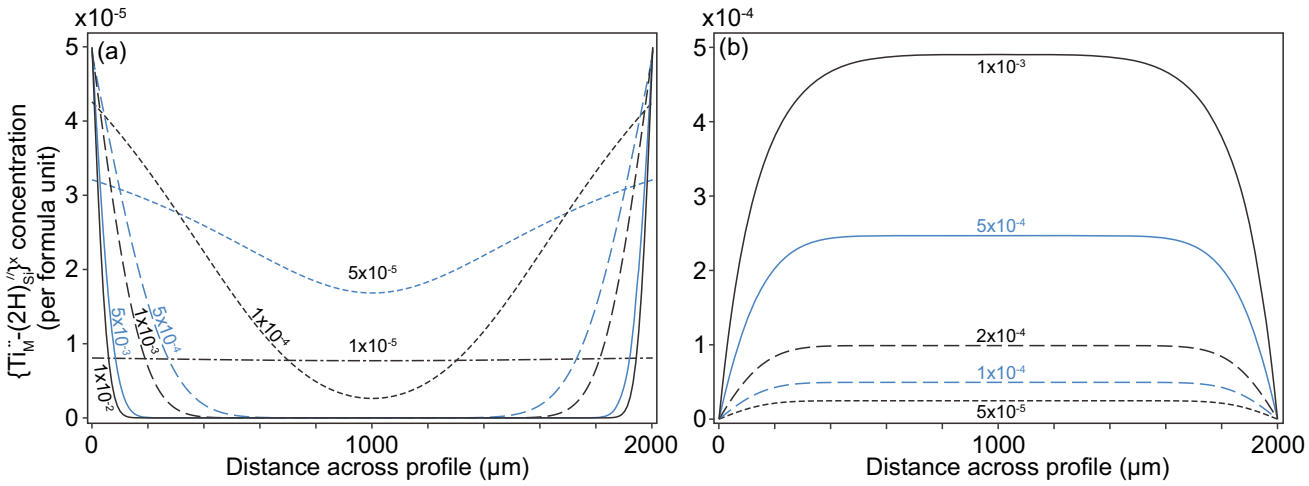

Fig. 3 The effect of changing **a** ∑Ti and **b** ∑H on profiles lengths and shapes. Only the $\{Ti_M^{\bullet\bullet} - (2H)_{Si}''\}^{\times}$ profiles are shown, for clarity. In **a**, annotations are the model ∑Ti. As ∑Ti increases, profile lengths become shorter. Concentrations are per formula unit. Model parameters are K: 10^5, ∑Ti (initial and boundary): 1×10^{-5} to 1×10^{-2} (~3 to 4000 wt. ppm), ∑H (initial): 1×10^{-8}, H (boundary): 1×10^{-4}, time: 86,400 s (24 h); dx: 10 µm, D^*: 10^{-11} m^2s^{-1}. In **b**, each curve represents a different initial H content (marked on curves). Model parameters are K: 10^5, ∑Ti (initial and boundary): 1×10^{-3} (~340 wt. ppm), ∑H (initial): 5×10^{-5} to 1×10^{-3} (~2 to 32 wt. ppm H_2O), ∑H (boundary): 1×10^{-8}, time: 86,400 s (24 h); dx: 10 µm, D^*: 10^{-11} m^2 s^{-1} (approximately equivalent to D* at 900 °C)

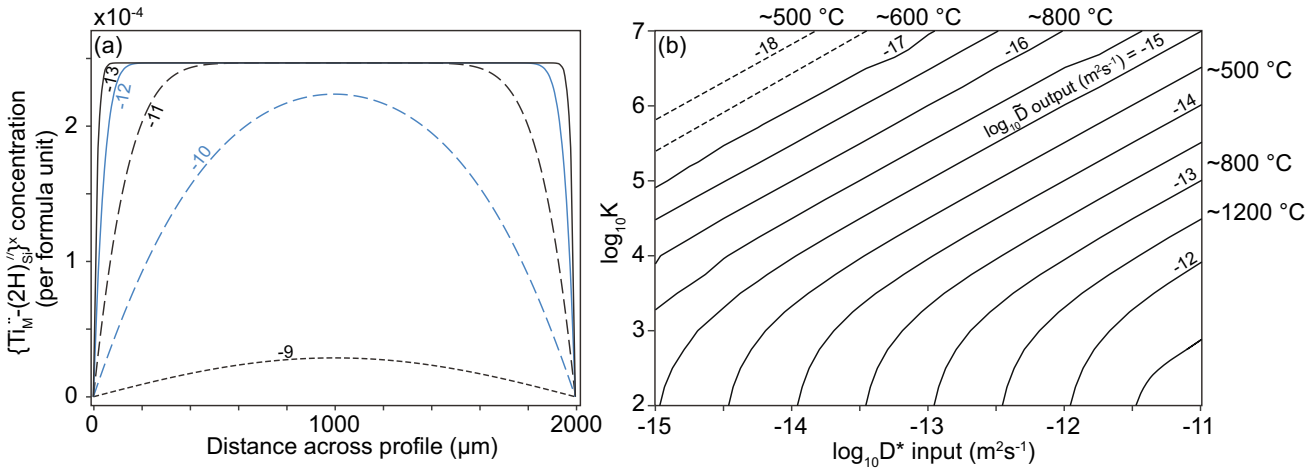

Fig. 4 The effect of changing the model input D^* on the output profiles of $\{Ti_M^{\bullet\bullet} - (2H)_{Si}''\}^{\times}$. Concentrations are per formula unit. **a** Model parameters are K: 10^5, $\sum$Ti (initial and boundary): 10^{-3}. $\sum$H (initial): 5×10^{-4}, $\sum$H (boundary): 10^{-8}, time: 86,400 s; dx: 10 μm, D^*: 10^{-11} m^2 s^{-1}. **b** Results of models (output diffusion coefficients $\tilde{D}$ from fits to $\{Ti_M^{\bullet\bullet} - (2H)_{Si}''\}^{\times}$ profiles) run with different D^* and K inputs. Solid lines are contours of model outputs, dashed lines are estimates. Approximate temperatures are added, based on the model outputs (see below), e.g., at 800 °C, $K \approx 10^5$ and $D^* \approx 10^{-12}$ m^2 s^{-1}, albeit with considerable uncertainties associated with the choice of absorption coefficients. The minor aberrations in some contours are likely related to (1) extracting $\tilde{D}$ using an analytical solution to Fick's second law which assumes an error function form, for profiles which deviate from this form at extreme K values and (2) numerical inaccuracies at low D^*, i.e., Δx may be too large to resolve short profiles at certain combinations of D^* and K

of the concentration–time curves are relatively insensitive to Δx, even if the exact values outputted by the model are affected. Therefore, the D^*s from our modelling should be considered as more reliable than the concentrations (e.g., C_{rim}, $C_{initial}$), at least within the accuracy constraints associated with the absorption coefficients and other assumptions.

Profile shapes

The diffusion–reaction models can produce concentration−distance profiles that have forms consistent with error-function shapes (e.g., Figs. 2, 3, 4), i.e., as would be expected for one-dimensional, concentration−independent diffusion with constant boundary and initial conditions—the examples above generally show such behaviour. However, the models can also produce shapes that deviate considerably from error−function forms. One notable possibility is the formation of stepped-shaped profiles, which can form as a result of diffusion–reaction processes (e.g., Dohmen et al. 2010; Jollands et al. 2022). Whilst such profiles have not been observed in any of the H-in or H-out experiments in forsterite, it is worth considering that the model predicts that they could exist given specific combinations of K, D^* and Ti and H concentrations. An example is presented in the Supplementary Online Materials (Fig. S4).

Diffusion–reaction model outputs

Fits and profile shapes

Most data could be satisfactorily fitted using the models described above, although the model profile shapes sometimes deviated from the measured profiles. The quality of fit was different when different absorption coefficients were used.

Typical model fits are shown in Fig. 5. Each panel shows the concentration of different defects as a function of distance from the interface, or time, for both the data, which was resolved into individual defects and the model. Also shown are the model diffusion coefficients associated with $(2H)_M^{\times}$ and the diffusion coefficients extracted for the same data assuming simple diffusive behaviour (Eqs. A19–A21 in the Supplementary Online Material).

The first observation is that, in line with the qualitative description in the section above, profiles of all modelled defects can form through coupled diffusion and inter-site reaction, where diffusion is only associated with $(2H)_M^{\times}$. Secondly, they also show that such profiles can form at considerably higher concentration than that of the diffusing $(2H)_M^{\times}$ defect, which is present at much lower concentrations. Thirdly, in order to generate the high concentration profiles of defects formed by the reactions, the diffusion coefficient has to be considerably greater than that extracted from a simple fit to the curves, with the difference between $\tilde{D}$ and D^* being one to two orders of magnitude.

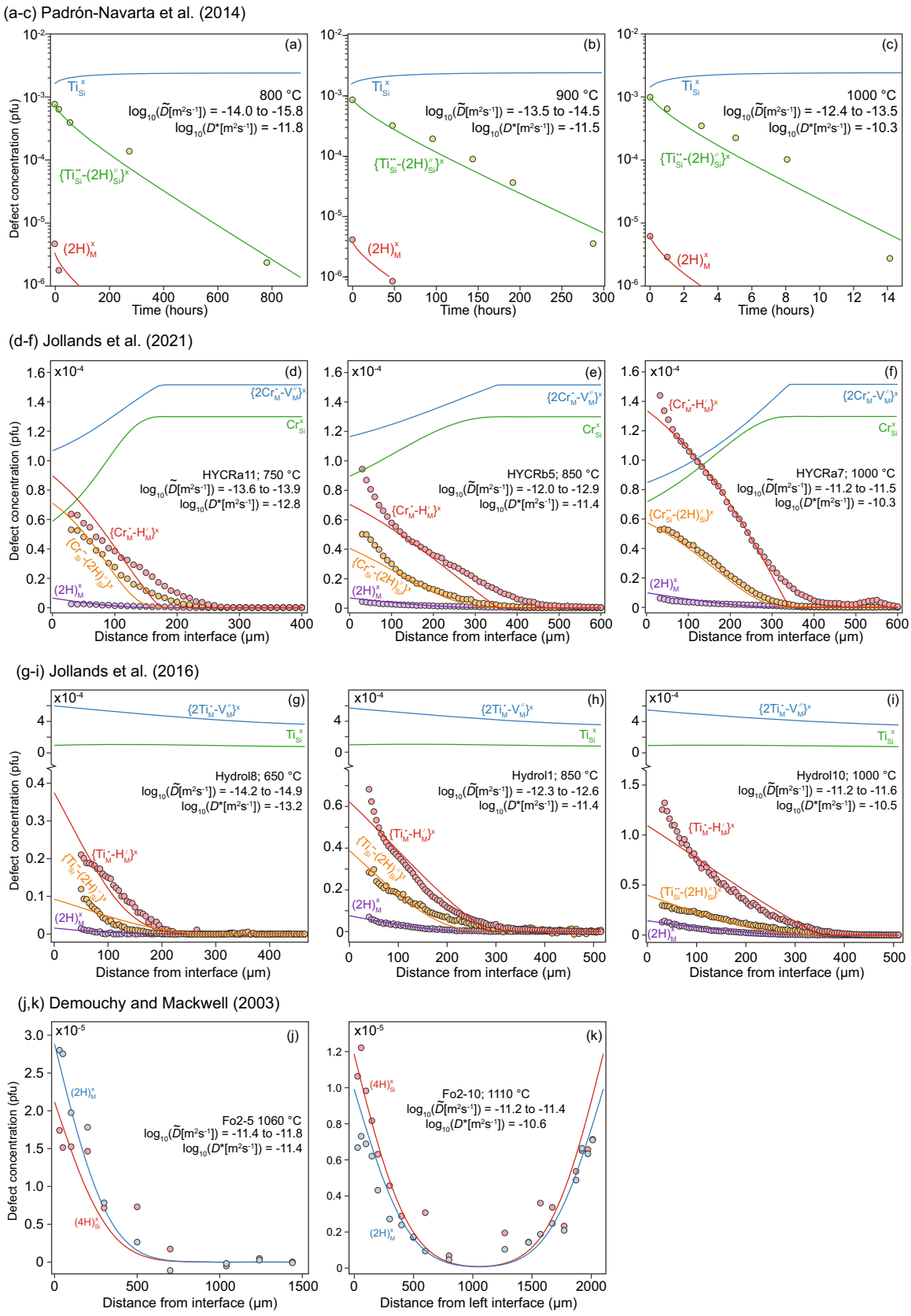

Fig. 5 Fits to the diffusion–reaction models for data from **a**–**c** Padrón-Navarta et al. (2014), **d**–**f** Jollands et al. (2021); **g**–**i** Jollands et al. (2016b); **j**, **k** Demouchy and Mackwell (2003). Solid lines are model fits

This is intuitive when qualitatively considered from the point of view of Fick's first law, which describes flux. If the flux is constant (broadly, the total amount of H passing into the crystal) and the concentration of the diffusing species is decreased (a low concentration of the $(2H)_M^\times$), then D^* must be increased to compensate. If these models are even qualitatively correct, then the diffusion coefficients extracted in the four previous studies of diffusion in forsterite are phenomenologically correct, but can be only considered as minima for the actual diffusivity of the $(2H)_M^\times$ defect.

Extracted D^*s, Ks and concentrations from diffusion–reaction models

Some model outputs are presented in Tables 3 and 4 and in Figs. 5, 6 and 7.

The concentrations of defects extracted using the diffusion–reaction method show order of magnitude agreement with those extracted using analytical solutions of Fick's second law (Table 4). A major difference is that, in the diffusion–reaction models, all defect concentrations are fit simultaneously, which tends to weight the fit to defects with higher concentrations, whereas the profiles associated with different defects would be fitted separately when using the analytical solutions. The result is that the poorest agreement between concentrations tends to be associated with the $(2H)_M^\times$ defect.

In terms of diffusion coefficients, the Demouchy and Mackwell (2003) D^*s do not agree with the other three, this is most likely due to the poorly constrained physical model and the unknown impurities contained in their (as-received) forsterite crystals. The agreement between the Padrón-Navarta et al. (2014) D^*s and both the Jollands et al. (2016b) and the Jollands et al (2021) D^*s is striking, considering that the published Padrón-Navarta et al. (2014) D^*s, assuming simple diffusion, were an order of magnitude slower than those determined by Jollands et al. (2016b) and Jollands et al. (2021).

Whilst the uncertainties in the modelling preclude derivation of an Arrhenius relationship ($D^* = D_0^* \exp(-E_a/(RT))$), estimated ranges of activation energy (E_a) and pre-exponential factor are (D_0^*) are 120 to 170 kJ mol^{-1} and 10^{-3} to $10^{-6.5}$ m^{2}s^{-1}, respectively (R is the gas constant (kJ mol^{-1} K^{-1}), T is absolute temperature (K)). Our calculation assumes that pressure effects are negligible and uses D^* values determined using the Libowitzky and Rossman (1997) and Withers et al. (2012) calibration.

The extracted K values are shown in Fig. 7a. The K associated with Eq. (1) (reaction forming $\{Ti_M^{\bullet\bullet} - (2H)_{Si}''\}^\times$) extracted from the Padrón-Navarta et al. (2014) data agrees

Table 3 D^* and K outputted from the diffusion–reaction model, using the Libowitzky and Rossman (1997)/Withers et al. (2012) calibration

Expt. ID	$\log_{10}K$		$\log_{10}(D^*$ [m^{2}s^{-1}])	$\log_{10}(\tilde{D}$ [m^{2}s^{-1}])
Demouchy and Mackwell (2003)				
	$2(2H)_M^\times + Si_{Si}^\times = (4H)_{Si}^\times + \{Si_i^{\bullet\bullet\bullet\bullet} - 2V_M''\}^\times$			
Fo2-5	− 0.4 [− 1.4,1.1]		− 11.4 [− 11.9,− 10.5]	− 11.4, − 11.8
Fo2-10	0.5 [− 0.9,1.5]		− 10.6 [− 11.0,-10.1]	− 11.2, − 11.4
Jollands et al. (2016a, b) ($Ti^{4+}/\sum Ti = 0.1$)				
	$Ti_{Si}^\times + (2H)_M^\times = \{Ti_M^{\bullet\bullet} - (2H)_{Si}''\}^\times$	$\{2Ti_M^\bullet - V_M''\}^\times + (2H)_M^\times = 2\{Ti_M^\bullet - H_M'\}^\times$		
Hydrol8	5.4 [5.0, 5.9]	− 0.6 [− 0.7, 0.5]	− 13.2 [− 13.7, − 13.0]	− 14.9, − 14.2
Hydrol1	5.1 [4.5, 5.4]	0.3 [0, 1.3]	− 11.4 [− 11.8, − 11.0]	− 12.6, − 12.3
Hydrol10	4.7 [4.4, 5.1]	0.5 [0.5, 1.5]	− 10.5 [− 10.6, − 9.7]	− 11.6, − 11.2
Jollands et al. (2021) ($Cr^{4+}/\sum Cr = 0.3$)				
	$Cr_{Si}^\times + (2H)_M^\times = \{Cr_M^{\bullet\bullet} - (2H)_{Si}''\}^\times$	$\{2Cr_M^\bullet - V_M''\}^\times + (2H)_M^\times = 2\{Cr_M^\bullet - H_M'\}^\times$		
HYCRa11	5.3 [4.8, 6.1]	1.1 [0.9, 2.3]	− 12.8 [− 12.8, − 12.2]	− 13.9, − 13.7
HYCRb5	5.1 [4.6, 5.5]	1.1 [1, 2.6]	− 11.4 [− 11.9, − 10.9]	− 12.9, − 12.5
HYCRa7	4.9 [4.6, 5.7]	1.3 [1.3, 2.9]	− 10.3 [− 10.6, − 9.8]	− 11.5, − 11.3
Padrón-Navarta et al. (2014)				
	$Ti_{Si}^\times + (2H)_M^\times = \{Ti_M^{\bullet\bullet} - (2H)_{Si}''\}^\times$			
800 °C	5.4 [5.0, 6.1]		− 11.8 [− 12.1, − 11.1]	− 15.8, − 14.0
900 °C	5.3 [5.0, 6.0]		− 11.5 [− 11.8, − 10.9]	− 14.5, − 13.5
1000 °C	5.2 [4.8, 6.0]		− 10.3 [− 10.7, − 9.7]	− 13.5, − 12.4

The numbers in brackets represent the minimum and maximum values derived using all absorption coefficients. Also shown is $\tilde{D}$ determined using analytical solutions, with the range representing values determined for different defects. All other model outputs are presented in the Supplementary Online Material.

Table 4 Interface or initial concentrations extracted from diffusion–reaction models, along with those extracted directly from experimental data using relevant analytical solutions of Fick's second law

Expt. ID	Analytical solution		Diffusion–reaction model	
Demouchy and Mackwell (2003)				
	$(4H)_{Si}^{\times}$	$(2H)_{M}^{\times}$	$(4H)_{Si}^{\times}$	$(2H)_{M}^{\times}$
Fo2-5	1.8×10^{-5}	3.1×10^{-5}	2.1×10^{-5}	3.4×10^{-5}
Fo2-10	8.2×10^{-6}	7.5×10^{-6}	1.2×10^{-5}	6.6×10^{-6}

Expt. ID	Analytical solution			Diffusion–reaction model		
Jollands et al. (2016a, b) ($Ti^{4+}/\sum Ti=0.1$)						
	$(2H)_{M}^{\times}$	$\{Ti_{M}^{\bullet}-H_{M}^{\prime}\}^{\times}$	$\{Ti_{M}^{\bullet\bullet}-(2H)_{Si}^{\prime\prime}\}^{\times}$	$(2H)_{Mg}^{\times}$	$\{Ti_{M}^{\bullet}-H_{M}^{\prime}\}^{\times}$	$\{Ti_{M}^{\bullet\bullet}-(2H)_{Si}^{\prime\prime}\}^{\times}$
Hydrol8	3.9×10^{-6}	2.3×10^{-5}	3.2×10^{-5}	1.6×10^{-6}	9.3×10^{-6}	3.7×10^{-5}
Hydrol1	9.0×10^{-6}	8.6×10^{-5}	3.8×10^{-5}	7.7×10^{-6}	6.2×10^{-5}	3.9×10^{-5}
Hydrol10	1.6×10^{-5}	1.5×10^{-4}	3.5×10^{-5}	1.4×10^{-5}	1.1×10^{-4}	4.0×10^{-5}

Expt. ID	Analytical solution			Diffusion–reaction model		
Jollands et al. (2021) ($Cr^{4+}/\sum Cr=0.3$)						
	$(2H)_{M}^{\times}$	$\{Cr_{M}^{\bullet}-H_{M}^{\prime}\}^{\times}$	$\{Cr_{M}^{\bullet\bullet}-(2H)_{Si}^{\prime\prime}\}^{\times}$	$(2H)_{M}^{\times}$	$\{Cr_{M}^{\bullet\bullet}-(2H)_{Si}^{\prime\prime}\}^{\times}$	$\{Cr_{M}^{\bullet}-H_{M}^{\prime}\}^{\times}$
HYCR11	3.6×10^{-6}	8.2×10^{-5}	7.7×10^{-5}	6.6×10^{-6}	9.0×10^{-5}	7.1×10^{-5}
HYCRb5	4.1×10^{-6}	9.2×10^{-5}	6.0×10^{-5}	4.9×10^{-6}	1.2×10^{-4}	8.2×10^{-5}
HYCR7	5.7×10^{-6}	1.6×10^{-4}	7.0×10^{-5}	8.4×10^{-6}	1.8×10^{-4}	1.0×10^{-4}

Expt. ID	Analytical solution		Diffusion–reaction model	
Padrón-Navarta et al. (2014) [initial concentrations]				
	$(2H)_{M}^{\times}$	$\{Ti_{M}^{\bullet\bullet}-(2H)_{Si}^{\prime\prime}\}^{\times}$	$(2H)_{M}^{\times}$	$\{Ti_{M}^{\bullet\bullet}-(2H)_{Si}^{\prime\prime}\}^{\times}$
800 °C	4.7×10^{-6}	7.8×10^{-4}	2.9×10^{-6}	7.9×10^{-4}
900 °C	4.2×10^{-6}	8.6×10^{-4}	3.9×10^{-6}	8.6×10^{-4}
1000 °C	5.9×10^{-6}	8.6×10^{-4}	6.0×10^{-6}	8.6×10^{-4}

The concentrations from the Padrón-Navarta et al. (2014) H-out experiments are initial, all others, from H-in experiments, are interface concentrations. All concentrations are presented as defect concentrations determined using the Libowitzky and Rossman (1997)/Withers et al. (2012) calibration

well with K for the same reaction from the Jollands et al. (2016b) data. This is again notable, given that both the physical model and experimental setups were different for in these two studies. These show that $\log_{10}K$ for Eq. (1) is positive over the studied temperature range and increases with decreasing temperature; thus, making $\{Ti_{M}^{\bullet\bullet}-(2H)_{Si}^{\prime\prime}\}^{\times}$ less stable at higher T. K associated with Eq. (3) (reaction forming $\{Cr_{M}^{\bullet\bullet}-(2H)_{Si}^{\prime\prime}\}^{\times}$) is similar to that associated with Eq. (1), with a similar slope. $\mathrm{Log}_{10}K$ associated with Eq. (4) (forming $\{Cr_{M}^{\bullet}-H_{M}^{\prime}\}^{\times}$) is positive over the studied temperature range and increases with increasing T, thus apparently making the $\{Cr_{M}^{\bullet}-H_{M}^{\prime}\}^{\times}$ defect more stable at higher T. K associated with Eq. (5), i.e., forming $\{Ti_{M}^{\bullet}-H_{M}^{\prime}\}^{\times}$ has broadly the same slope in K–T space as that associated with Eq. (4), but at lower values.

Absorption coefficients

The modelling presented above applied the slope of the Libowitzky and Rossman (1997) wavenumber-absorption coefficient relationship, pinned to the Withers et al. (2012) calibration. Applying a different absorption coefficient will change the concentrations, both relative and absolute, of defects, which will then change the fitted K and D^{*}. An example of this effect is shown in Fig. 8, which shows the results of refitting the Jollands et al. (2016b) dataset, using $Ti^{4+}/\sum Ti=0.1$ and different absorption coefficients. The differences in extracted $\tilde{D}$s is up to an order of magnitude at the 650 °C, with convergence at 950 °C. The K values are considerably different between calibrations, with no apparent convergence.

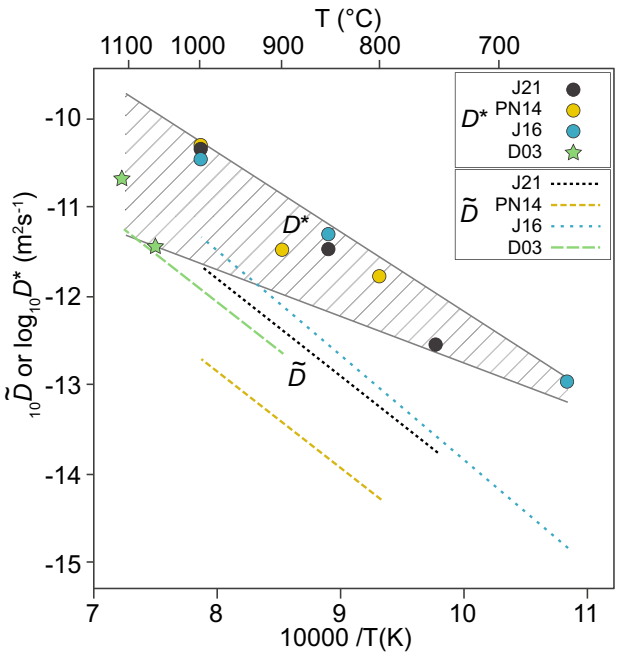

Fig. 6 Diffusion coefficients (D^*) extracted from diffusion–reaction modelling (circles) along with curves representing estimate lower and upper D^* limits (solid grey lines, hashed fill), used to extract possible ranges of activation energy and pre-exponential factor (see text). Note especially the ~ 1.5 log unit difference between PN14 and J16/J21 $\tilde{D}$s, versus the good agreement between the respective D^*s. D03: Demouchy and Mackwell (2003); PN14: Padrón-Navarta et al. (2014); J16: Jollands et al. (2016a, b); J21: Jollands et al. (2021)

Δ*G* and *K* from DFT modelling

Calculated values of the Δ*G* and *K* for each reaction are presented in Table 5 and Fig. 7b, for conditions specifically associated with the experiments in question. The Δ*G* values for the reactions are all negative. The Δ*G* for the reactions associated with trivalent cations are less negative (~ − 10 to − 35 kJ mol^{-1}) relative to those associated with tetravalent cations (~ − 100 to − 130 kJ mol^{-1}). The values of *K* increase with decreasing temperature for all reactions except that forming $\{Cr^{\bullet}_{M} - H'_{M}\}^{\times}$, which shows the opposite slope (Fig. 7).

Discussion

Diffusion–reaction modelling vs. DFT calculations

The DFT calculations are especially useful as they provide an independent constraint on the *K*s determined by diffusion–reaction modelling. The relative *K*s for the reactions forming the two classes of H-bearing defects agree between the two methods—*K*s associated with the formation of the 'clinohumite-type' defects are consistently higher than for with reactions involving trivalent cations (Fig. 9).

In general, there is reasonable first-order agreement between the DFT-calculated *K*s and those extracted from diffusion–reaction modelling, for the reactions forming the clinohumite-type defects ($\{Ti^{\bullet\bullet}_{M} - (2H)''_{Si}\}^{\times}$ and $\{Cr^{\bullet\bullet}_{M} - (2H)''_{Si}\}^{\times}$, Eqs. (1) and (3)), both in terms of slope in *T*–*K* space and absolute values (Figs. 7, 8). Therefore, we can state with some confidence that the stability of the $\{Ti^{\bullet\bullet}_{M} - (2H)''_{Si}\}^{\times}$ and $\{Cr^{\bullet\bullet}_{M} - (2H)''_{Si}\}^{\times}$ defects decrease with increasing temperature. However, the agreement between the *K*s associated with the formation of the $\{Cr^{\bullet}_{M} - H'_{M}\}^{\times}$ and $\{Ti^{\bullet}_{M} - H'_{M}\}^{\times}$ defects is poor—there is a ~ 3 orders of magnitude difference between the values associated with the DFT and diffusion–reaction models. Moreover, the *T*–*K* slope of the reaction forming the $\{Cr^{\bullet}_{M} - H'_{M}\}^{\times}$ defect is opposite according to the two models.

The good agreement between the *K*s of the reactions forming the 'clinohumite-type' defects is encouraging, but the disagreement associated with the reactions forming the trivalent-associated defects is clearly problematic. We do not have a firm explanation for this.

One possibility is the assumption of full binding between the different species in the $\{Cr^{\bullet}_{M} - H'_{M}\}^{\times}$, $\{2Cr^{\bullet}_{M} - V''_{M}\}^{\times}$, etc. defects, which is implicit in the diffusion–reaction model. This was a simplifying assumption made for the purposes of diffusion–reaction modelling, but is certainly incorrect. Blanchard et al. (2017) calculated that there are at least two $\{Cr^{\bullet}_{M} - H'_{M}\}^{\times}$ defects with similar energies and considerations of trivalent cation incorporation into divalent sites would suggest that a defect with $\{2Cr^{\bullet}_{M} - V''_{M}\}^{\times}$ stoichiometry can also be written as $\{Cr^{\bullet}_{M} - V''_{M}\}' + Cr^{\bullet}_{M}$ (partially bound) or $2Cr^{\bullet}_{M} + V''_{M}$ (unbound), with the proportion of bound pairs dependent to some extent on T, Cr concentration and the relevant binding energy. If we fully unbind the $\{Cr^{\bullet}_{M} - H'_{M}\}^{\times}$ defect to $Cr^{\bullet}_{M} + H'_{M}$ and $\{2Cr^{\bullet}_{M} - V''_{M}\}^{\times}$ to $2Cr^{\bullet}_{M} + V''_{M}$ in the DFT calculations for Eq. (4), $\log_{10}K$ drops considerably, from 2.55 down to − 22.60. The true value should lie between these end-members (e.g., Jollands et al. 2018). Clearly, this requires further consideration, but this may be a reason for the first-order disagreement between the DFT and diffusion–reaction models for the reactions associated with trivalent cations.

In addition, in our modelling we only expressly considered the high temperature energy of the most enthalpically stable arrangement of the $\{Cr^{\bullet}_{M} - H'_{M}\}^{\times}$ defect-strictly the high temperature energy of all arrangements should be considered. This can only serve to increase *K* (and with it the mismatch between our calculations and experiments) as if a neglected arrangement has lower energy at high temperatures than our calculated arrangement, $\{Cr^{\bullet}_{M} - H'_{M}\}^{\times}$ will be more favoured and *K* will be increased.

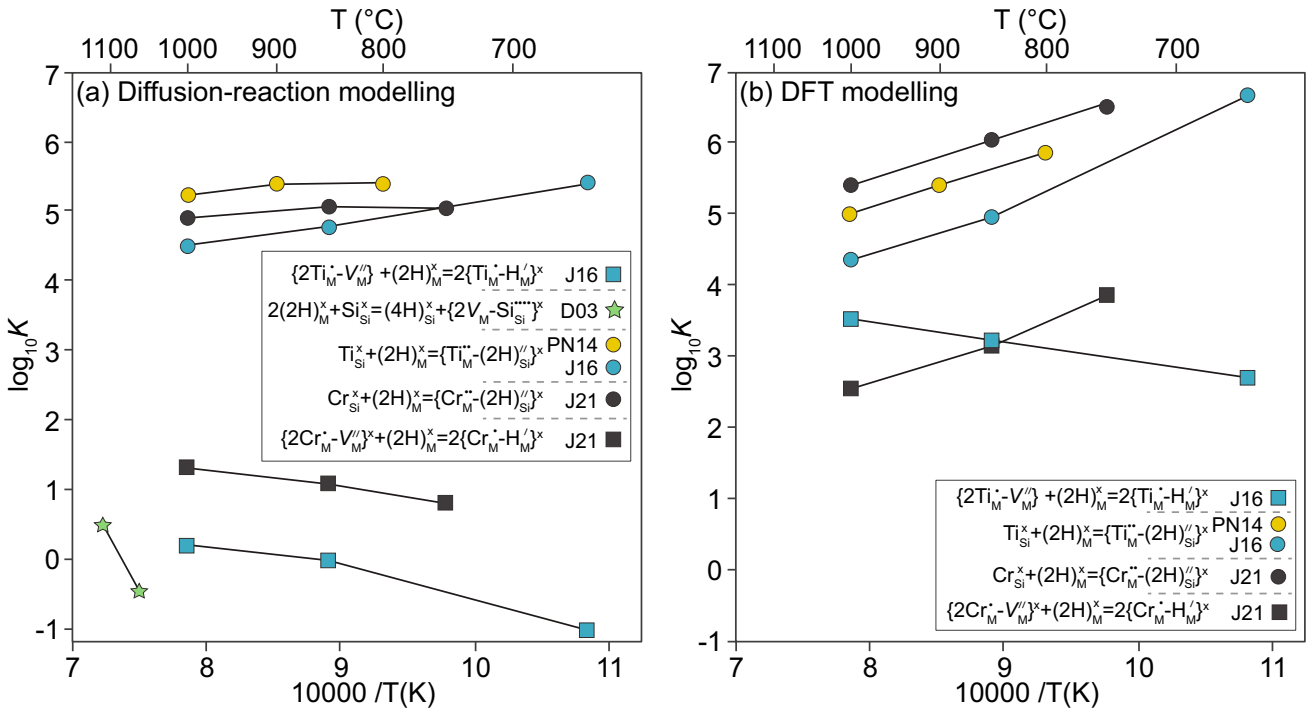

Fig. 7 Equilibrium constants (K) extracted from both diffusion–reaction and DFT modelling. Uncertainties are not presented—any potential uncertainties associated with curve fitting are subsumed by those related to absorption coefficients/model size/trace element content. See the Supplementary Online Material for further information. **a** K extracted from diffusion–reaction modelling, for the five reactions considered in the text. Lines between points are provided for visual guidance only. PN14: Padrón-Navarta et al. (2014); J16: Jollands et al. (2016b); D03: Demouchy and Mackwell (2003); J21: Jollands et al. (2021). **b** K extracted from DFT modelling. The references to J16, PN14, etc. refer to the concentrations of H_2O, Ti, Cr used in the models. e.g., the points labelled as J21 were calculated using 50 wt. ppm Cr^{4+} and 15 wt. ppm H_2O

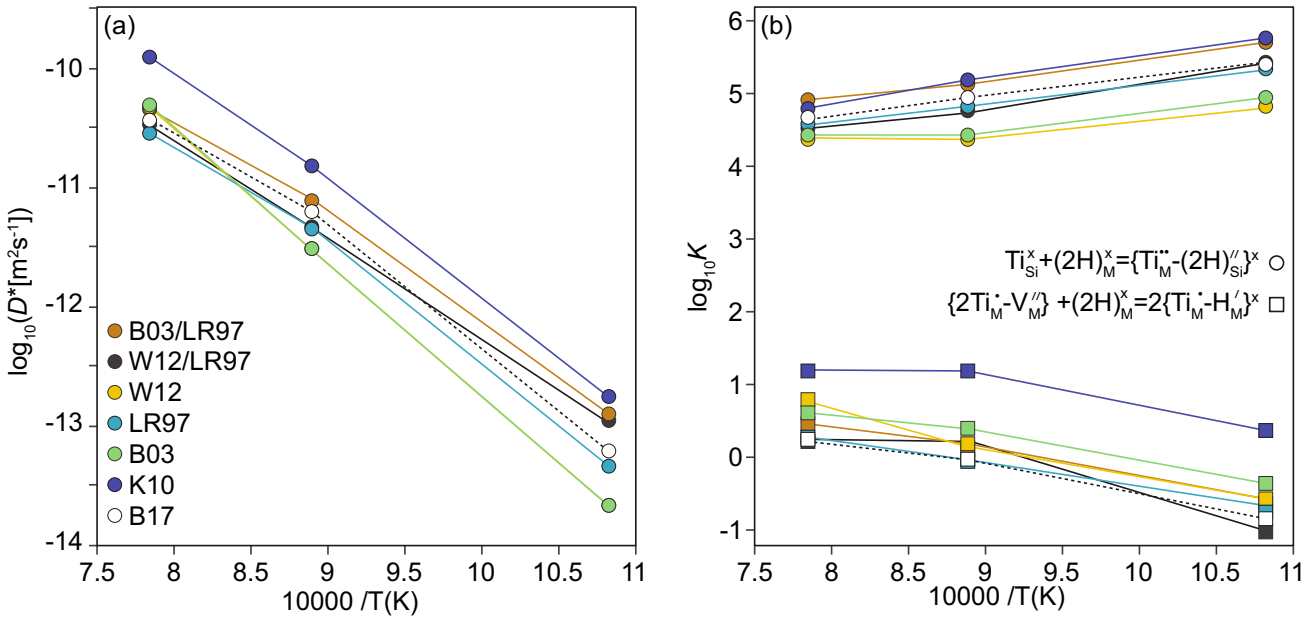

Fig. 8 The effect of different absorption coefficients on the outputs of diffusion–reaction models, for the Ti-doped forsterite experiments of Jollands et al. (2016b). **a** D^* as a function of inverse temperature, showing around one order of magnitude difference between D^* extracted using different absorption coefficients. **b** K for the two reactions as a function of inverse temperature, again showing considerable variation between Ks determined with different absorption coefficients. W12: Withers et al. (2012); LR97: Libowitzky and Rossman (1997); B03: Bell et al. (2003); K10: Kovács et al. (2010); B17: Blanchard et al. (2017)

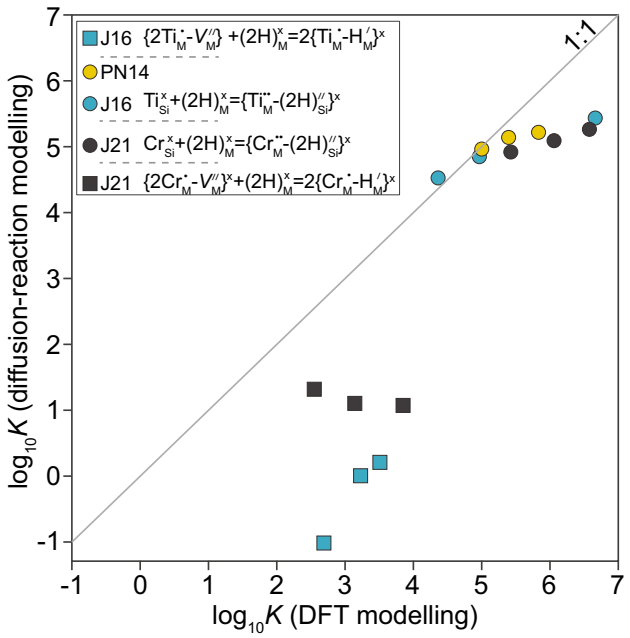

Fig. 9 *K* determined by diffusion–reaction modelling versus the same determined by DFT modelling (data in Fig. 7a vs. data in Fig. 7b)

Mobility of hydrated M-site vacancies

According to the model outputs, the diffusivity of the $(2H)^{\times}_{M}$ defect is greater than previously determined by up to 2 orders of magnitude over the studied temperature range. Within the framework of the model assumptions, these extracted diffusion coefficients are best guesses of the true mobility of $(2H)^{\times}_{M}$. In these diffusion experiments, the true mobility of $(2H)^{\times}_{M}$ is not expressed in the resulting profiles, which are always considerably shorter than profiles that would be expected from applying the relevant diffusivity in isolation. This is because the mobile defects are continuously rate-limited by inter-site reactions. The diffusivities that have been measured (Demouchy and Mackwell, 2003; Jollands et al. 2016b, 2021; Padrón-Navarta et al. 2014), are, however, (likely) useful for practical purposes if the experimental calibration is broadly matched to the natural sample.

This prediction of high $(2H)^{\times}_{M}$ diffusivity can be tested by conducting H−^{2}H exchange experiments in extremely pure forsterite, at high $aSiO_2$ conditions. This means experiments in which a crystal is fully equilibrated with H (or ^{2}H) at exactly the same P, T, fH_2O, fO_2, $aSiO_2$ conditions as a subsequent short-duration diffusion anneal. This is non-trivial, however, as the initial step may require an anneal with a duration of weeks to months.

Table 5 Defect energies and *K* calculated using DFT

T (°C)	P (GPa)	Trace element (wt. ppm)	H_2O (wt. ppm)	Equivalent expt. ID	Reaction energy (ΔG)		$\log_{10}K$ (DFT)	$\log_{10}K$ (diff-reac)
					eV	kJ mol^{-1}		
$Ti^{\times}_{Si} + (2H)^{\times}_{M} = \{Ti^{\bullet\bullet}_{M} - (2H)''_{Si}\}^{\times}$								
650	1.5	Ti^{4+}, 30	15	J16, Hydrol8	− 1.22	− 118.2	6.69	5.16
850	1.5	Ti^{4+}, 30	15	J16, Hydrol10	− 1.11	− 106.6	4.96	4.73
1000	1.5	Ti^{4+}, 30	15	J16, Hydrol10	− 1.10	− 106.2	4.36	4.47
800	0	Ti^{4+}, 600	100	P14, 800	− 1.10	− 105.8	5.84	5.22
900	0	Ti^{4+}, 600	100	P14, 900	− 1.10	− 105.7	5.40	5.14
1000	0	Ti^{4+}, 600	100	P14, 1000	− 1.09	− 105.2	5.01	4.96
$Cr^{\times}_{Si} + (2H)^{\times}_{M} = \{Cr^{\bullet\bullet}_{M} - (2H)''_{Si}\}^{\times}$								
750	1.5	Cr^{4+}, 50	15	J21, HYCRa11	− 1.33	− 128.7	6.57	5.27
850	1.5	Cr^{4+}, 50	15	J21, HYCRb5	− 1.35	− 130.2	6.05	5.08
1000	1.5	Cr^{4+}, 50	15	J21, HYCRa7	− 1.36	− 131.6	5.4	4.91
$\{2Cr^{\bullet}_{M} - V''_{M}\}^{\times} + (2H)^{\times}_{M} = 2\{Cr^{\bullet}_{M} - H'_{M}\}^{\times}$								
750	1.5	Cr^{3+}, 110	15	J21, HYCRa11	− 0.78	− 75.4	3.85	1.06
850	1.5	Cr^{3+}, 110	15	J21, HYCRb5	− 0.70	− 67.9	3.16	1.11
1000	1.5	Cr^{3+}, 110	15	J21, HYCRa7	− 0.64	− 62.2	2.55	1.33
$\{2Ti^{\bullet}_{M} - V''_{M}\}^{\times} + (2H)^{\times}_{M} = 2\{Ti^{\bullet}_{M} - H'_{M}\}^{\times}$								
650	1.5	Ti^{3+}, 300	5	J16, Hydrol8	− 0.55	− 53.1	2.71	− 1.04
850	1.5	Ti^{3+}, 300	10	J16, Hydrol10	− 0.72	− 69.6	3.24	− 0.05
1000	1.5	Ti^{3+}, 300	15	J16, Hydrol10	− 0.89	− 85.7	3.51	0.18

The *T*, *P*, Cr, Ti and H_2O contents used for each calculation are presented, as well as the ID of the equivalent experiment. Reaction energies are presented both in eV and kJ mol^{-1}, along with the relevant *K*. Also shown are the *K* values from diffusion–reaction modelling, for comparison

Conclusions, implications and model limitations

This study has presented a methodological framework for considering H diffusion in forsterite. This should hopefully provide a starting point for future modelling.

Overall, if we assume that the only H-bearing defect capable of diffusing any appreciable distance (> 10 s µm) in pure forsterite (in minutes to weeks at < 1000 °C) is the hydrated metal vacancy $(2H)^{\times}_{M}$, then, based simply on considerations of diffusive flux, the diffusivity of this defect (D^{*}) must be greater than the diffusivity extracted by fitting experimental data to simple solutions of Fick's second law ($\tilde{D}$). The progress of $(2H)^{\times}_{M}$ defects, as they move through the crystal, is slowed by inter-site reactions forming other defects. Whilst there are considerable caveats, we estimate the diffusivity of $(2H)^{\times}_{M}$ to be ~ 1–2 orders of magnitude greater than the previously measured diffusivity $\tilde{D}$. Such behaviour is proposed to have been observed in all H-in and H-out experimental studies using forsterite. Along with the upwards revision of diffusivities, this appears to reconcile some previously disparate experimental results. This methodological development implemented in our model should be built on moving forwards.

Finally, the following is a non-exhaustive list of the limitations of our model, which should be noted when critically considering the implications and that should be addressed as the methodology improves and/or more experimental data becomes available. These have been placed into a hierarchy based on their potential importance.

1. The model outputs are highly dependent on absorption coefficients. In previous H diffusion studies, it has been reasonable to simply use integrated absorbance of any band to extract a diffusion coefficient, without converting the absorbance to wt. ppm H_2O or similar. In diffusion–reaction models, this is no longer reasonable—absolute concentrations must be known. As an aside, it is also necessary to standardise baseline correction routines for FTIR spectra—absorption coefficients are only applicable if baseline corrections are always performed in the same way.
2. In the diffusion–reaction models, the reactions are considered in isolation, without intrinsic defect-forming reactions. As above, this will add considerable complexity to the models and will require a series of extra unconstrained terms.
3. In the DFT models, we assume a single configuration of each defect, whereas several may be (and almost certainly are) present.
4. The model is entirely based on the assumption that the only mobile defect is $(2H)^{\times}_{M}$ and that all H-bearing defects are detected by FTIR spectroscopy and present in the OH stretching region, i.e., no molecular H_2 (e.g., Moine et al. 2020) nor interstitial H weakly or not bounded to O. This assumption is, however, in line with thermodynamic modelling (Muir et al. 2022). Another possibility that we have not considered is whether a 'proton-polaron' type diffusion mechanism could occur in a crystal doped with only trace amounts of redox variable elements, e.g., $Cr^{2+}/^{3+}/^{4+}$ in the Jollands et al. (2021) study.
5. Whilst results from DFT modelling generally support the use of a diffusion–reaction model for the 'clinohumite-type' defects (both Cr and Ti), the calculated K values for defects associated with trivalent ions are inconsistent in terms of absolute values between diffusion–reaction and DFT models. However, the Ks determined by DFT modelling are highly dependent on whether the relevant defects are bound or unbound.
6. We assume K is constant at all points along diffusion profiles and has no dependence on concentration (Henry's law) which may not be a reasonable assumption. Adding a variable K to the model will again lead to considerable increase in complexity, which is unjustified.
7. Models often show profile shapes that are not consistent with the measured profiles, including near-linear concentration decreases instead of the measured error function forms.
8. Several of the defects in the Jollands et al. (2021) experiments are not considered (notably $(4H)^{\times}_{Si}$). The $(4H)^{\times}_{Si}$ defect is also omitted from the model describing the Padrón-Navarta et al. (2014) data. The justification is that the diffusivity of this defect is relatively low, therefore it is irrelevant over the time scales of these models. However, the interaction of this defect with any other defects will modify their concentrations, which will then modify the concentrations of many other defects.
9. We cannot provide a fully satisfactory explanation for why Jollands et al. (2021) and Demouchy and Mackwell (2003) both observed the $(4H)^{\times}_{Si}$ bands, whereas Jollands et al. (2016b) did not. One possibility is that the starting materials of Demouchy and Mackwell (2003) and Jollands et al. (2021) were previously equilibrated/grown in low $a\mathrm{SiO_2}$ systems, whereas the Jollands et al. (2016b) crystals were pre-equilibrated in the presence of $Mg_2Si_2O_6$.
10. Similarly, we do not provide a satisfactory explanation for the reaction that forms $(4H)^{\times}_{Si}$ in the Demouchy and Mackwell (2003) experiments. Repeat experiments using extremely pure forsterite crystals with well constrained trace element concentrations will be invaluable.

11. We assume that ∑Ti is constant in the Padrón-Navarta et al. (2014) experiments, but this does not account for their observation that Ti–rich phases exsolved from the forsterite.

Supplementary Information The online version contains supplementary material available at https://doi.org/10.1007/s00410-022-01954-1.

Acknowledgements Funding for this study came from a Swiss National Science Foundation Postdoc Mobility grant to MCJ (P400P2_183872). JAPN acknowledges financial support from the Spanish MICINN through the Ramón y Cajal fellowship (RYC2018-024363-I) funded by MICIN/AEI/10.13039/501100011033 and the FSE program "FSE invierte en tu futuro". JMRM acknowledges funding from National Natural Science Foundation of China (42050410319) and the Science and Technology Foundation of Guizhou Province (ZK2021-205). Thanks go to three anonymous referees for constructive and comprehensive reviews.

References

Aizawa Y, Barnhoorn A, Faul UH, FitzGerald JD, Jackson I, Kovács I (2008) Seismic properties of Anita Bay dunite: an exploratory study of the influence of water. J Petrol 49:841–855. https://doi.org/10.1093/petrology/egn007

Balan E, Ingrin J, Delattre S, Kovács I, Blanchard M (2011) Theoretical infrared spectrum of OH-defects in forsterite. Eur J Mineral 23:285–292. https://doi.org/10.1127/0935-1221/2011/0023-2090

Barth A, Newcombe M, Plank T, Gonnermann H, Hajimirza S, Soto GJ, Saballos A, Hauri E (2019) Magma decompression rate correlates with explosivity at basaltic volcanoes—constraints from water diffusion in olivine. J Volcanol Geotherm Res 387:106664. https://doi.org/10.1016/j.jvolgeores.2019.106664

Bell DR, Rossman GR, Maldener J, Endisch D, Rauch F (2003) Hydroxide in olivine: a quantitative determination of the absolute amount and calibration of the IR spectrum. J Geophys Res Solid Earth 108:2015. https://doi.org/10.1029/2001JB000679

Berry AJ, Hermann J, O'Neill HSC, Foran GJ (2005) Fingerprinting the water site in mantle olivine. Geology 33:869–872. https://doi.org/10.1130/G21759.1

Berry AJ, O'Neill HSC, Hermann J, Scott DR (2007a) The infrared signature of water associated with trivalent cations in olivine. Earth Planet Sci Lett 261:134–142. https://doi.org/10.1016/j.epsl.2007.06.021

Berry AJ, Walker AM, Hermann J, O'Neill HSC, Foran GJ, Gale JD (2007b) Titanium substitution mechanisms in forsterite. Chem Geol 242:176–186. https://doi.org/10.1016/j.chemgeo.2007.03.010

Blanchard M, Ingrin J, Balan E, Kovács I, Withers AC (2017) Effect of iron and trivalent cations on OH defects in olivine. Am Mineral 102:302–311. https://doi.org/10.2138/am-2017-5777

Brodholt JP, Refson K (2000) An ab initio study of hydrogen in forsterite and a possible mechanism for hydrolytic weakening. J Geophys Res Solid Earth 105:18977–18982. https://doi.org/10.1029/2000JB900057

Burnham A, O'Neill HSC (2020) Mineral–melt partition coefficients and the problem of multiple substitution mechanisms: insights from the rare earths in forsterite and protoenstatite. Contrib Mineral Petrol 175:7. https://doi.org/10.1007/s00410-019-1636-9

Causey RA, Karnesky RA, San Marchi C (2012) 4.16—tritium barriers and tritium diffusion in fusion reactors. In: Konings RJM (ed) Comprehensive nuclear materials. Elsevier, Oxford, pp 511–549. https://doi.org/10.1016/B978-0-08-056033-5.00116-6

Chakraborty S (1997) Rates and mechanisms of Fe–Mg interdiffusion in olivine at 980 °C–1300 °C. J Geophys Res Solids Earth 102:12317–12331. https://doi.org/10.1029/97JB00208

Chakraborty S, Farver JR, Yund RA, Rubie DC (1994) Mg tracer diffusion in synthetic forsterite and San-Carlos olivine as a function of P, T and fO_2. Phys Chem Miner 21:489–500. https://doi.org/10.1007/BF00203923

Chen J, Inoue T, Weidner DJ, Wu Y, Vaughan MT (1998) Strength and water weakening of mantle minerals, olivine, wadsleyite and ringwoodite. Geophys Res Lett 25:575–578. https://doi.org/10.1029/98GL00043

Chen S, Hiraga T, Kohlstedt DL (2006) Water weakening of clinopyroxene in the dislocation creep regime. J Geophys Res Solid Earth 111:B08203. https://doi.org/10.1029/2005JB003885

Cherniak DJ, Liang Y (2014) Titanium diffusion in olivine. Geochim Cosmochim Acta 147:43–57. https://doi.org/10.1016/j.gca.2014.10.016

Clark SJ, Segall MD, Pickard CJ, Hasnip PJ, Probert MI, Refson K, Payne MC (2005) First principles methods using CASTEP. Z Krist Cryst Mater 220:567–570. https://doi.org/10.1524/zkri.220.5.567.65075

Cline CJ, Faul UH, David EC, Berry AJ, Jackson I (2018) Redox-influenced seismic properties of upper-mantle olivine. Nature 555:355–358. https://doi.org/10.1038/nature25764

Colson RO, McKay GA, Taylor LA (1989) Charge balancing of trivalent trace elements in olivine and low-Ca pyroxene: a test using experimental partitioning data. Geochim Cosmochim Acta 53:643–648. https://doi.org/10.1016/0016-7037(89)90007-0

Coogan LA, Saunders AD, Wilson RN (2014) Aluminum-in-olivine thermometry of primitive basalts: evidence of an anomalously hot mantle source for large igneous provinces. Chem Geol 368:1–10. https://doi.org/10.1016/j.chemgeo.2014.01.004

Costa F, Chakraborty S (2008) The effect of water on Si and O diffusion rates in olivine and implications for transport properties and processes in the upper mantle. Phys Earth Planet Inter 166:11–29. https://doi.org/10.1016/j.pepi.2007.10.006

Crank J (1975) The mathematics of diffusion. Oxford University Press, Oxford

Crépisson C, Blanchard M, Bureau H, Sanloup C, Withers AC, Khodja H, Surblé S, Raepsaet C, Béneut K, Leroy C, Giura P, Balan E (2014a) Clumped fluoride-hydroxyl defects in forsterite: implications for the upper-mantle. Earth Planet Sci Lett 390:287–295. https://doi.org/10.1016/j.epsl.2014.01.020

Crépisson C, Bureau H, Blanchard M, Ingrin J, Balan E (2014b) Theoretical infrared spectrum of partially protonated cationic vacancies in forsterite. Eur J Mineral 26:203–210. https://doi.org/10.1127/0935-1221/2014/0026-2366

Dai L, Karato SI (2014) High and highly anisotropic electrical conductivity of the asthenosphere due to hydrogen diffusion in olivine. Earth Planet Sci Lett 408:79–86. https://doi.org/10.1016/j.epsl.2014.10.003

Dai L, Karato SI (2020) Electrical conductivity of Ti-bearing hydrous olivine aggregates at high temperature and high pressure. J Geophys Res Solid Earth 125(10):e2020JB020309. https://doi.org/10.1029/2020JB020309

Demouchy S, Mackwell S (2003) Water diffusion in synthetic iron-free forsterite. Phys Chem Miner 30:486–494. https://doi.org/10.1007/s00269-003-0342-2

Demouchy S, Mackwell S (2006) Mechanisms of hydrogen incorporation and diffusion in iron-bearing olivine. Phys Chem Miner 33:486–494. https://doi.org/10.1007/s00269-006-0081-2

Demouchy S, Tommasi A, Barou F, Mainprice D, Cordier P (2012) Deformation of olivine in torsion under hydrous conditions. Phys Earth Planet Inter 202:56–70. https://doi.org/10.1016/j.pepi.2012.05.001

Dohmen R, Chakraborty S (2007) Fe–Mg diffusion in olivine II: point defect chemistry, change of diffusion mechanisms and a model for calculation of diffusion coefficients in natural olivine. Phys Chem Miner 34:409–430. https://doi.org/10.1007/s00269-007-0158-6

Dohmen R, Becker HW, Chakraborty S (2007) Fe–Mg diffusion in olivine I: experimental determination between 700 and 1200 °C as a function of composition, crystal orientation and oxygen fugacity. Phys Chem Miner 34:389–407. https://doi.org/10.1007/s00269-007-0157-7

Dohmen R, Kasemann SA, Coogan L, Chakraborty S (2010) Diffusion of Li in olivine. Part I: experimental observations and a multi species diffusion model. Geochim Cosmochim Acta 74:274–292. https://doi.org/10.1016/j.gca.2009.10.016

Du Frane WL, Tyburczy JA (2012) Deuterium–hydrogen exchange in olivine: implications for point defects and electrical conductivity. Geochem Geophys Geosyst 13:Q03004. https://doi.org/10.1029/2011GC003895

Evans TM, O'Neill HSC, Tuff J (2008) The influence of melt composition on the partitioning of REEs, Y, Sc, Zr and Al between forsterite and melt in the system CMAS. Geochim Cosmochim Acta 72:5708–5721. https://doi.org/10.1016/j.gca.2008.09.017

Faul UH, Cline CJ, David EC, Berry AJ, Jackson I (2016) Titanium-hydroxyl defect-controlled rheology of the Earth's upper mantle. Earth Planet Sci Lett 452:227–237. https://doi.org/10.1016/j.epsl.2016.07.016

Fei H, Koizumi S, Sakamoto N, Hashiguchi M, Yurimoto H, Marquardt K, Miyajima N, Katsura T (2018) Mg lattice diffusion in iron-free olivine and implications to conductivity anomaly in the oceanic asthenosphere. Earth Planet Sci Lett 484:204–212. https://doi.org/10.1016/j.epsl.2017.12.020

Ferriss E, Plank T, Newcombe M, Walker D, Hauri E (2018) Rates of dehydration of olivines from San Carlos and Kilauea Iki. Geochim Cosmochim Acta 242:165–190. https://doi.org/10.1016/j.gca.2018.08.050

Garrido CJ, López Sánchez-Vizcaíno V, Gómez-Pugnaire MT, Trommsdorff V, Alard O, Bodinier J-L, Godard M (2005) Enrichment of HFSE in chlorite-harzburgite produced by high-pressure dehydration of antigorite-serpentinite: implications for subduction magmatism. Geochem Geophys Geosyst. https://doi.org/10.1029/2004GC000791

Grant KJ, Wood BJ (2010) Experimental study of the incorporation of Li, Sc, Al and other trace elements into olivine. Geochim Cosmochim Acta 74:2412–2428. https://doi.org/10.1016/j.gca.2010.01.015

Grützner T, Kohn SC, Bromiley DW, Rohrbach A, Berndt J, Klemme S (2017) The storage capacity of fluorine in olivine and pyroxene under upper mantle conditions. Geochim Cosmochim Acta 208:160–170. https://doi.org/10.1016/j.gca.2017.03.043

Hermann J, O'Neill HSC, Berry AJ (2005) Titanium solubility in olivine in the system TiO_2–MgO–SiO_2: no evidence for an ultra-deep origin of Ti-bearing olivine. Contrib Mineral Petrol 148:746–760. https://doi.org/10.1007/s00410-004-0637-4

Hermann J, Fitz Gerald JD, Malaspina N, Berry AJ, Scambelluri M (2007) OH-bearing planar defects in olivine produced by the breakdown of Ti-rich humite minerals from Dabie Shan (China). Contrib Mineral Petrol 153(4):417–428. https://doi.org/10.1007/s00410-006-0155-7

Hier-Majumder S, Anderson IM, Kohlstedt DL (2005) Influence of protons on Fe–Mg interdiffusion in olivine. J Geophys Res Solid Earth 110:B02202. https://doi.org/10.1029/2004JB003292

Hughes L, Pawley A (2019) Fluorine partitioning between humite-group minerals and aqueous fluids: implications for volatile storage in the upper mantle. Contrib Mineral Petrol 174:78. https://doi.org/10.1007/s00410-019-1614-2

Ingrin J, Blanchard M (2006) Diffusion of hydrogen in minerals. Rev Mineral Geochem 62:291–320. https://doi.org/10.2138/rmg.2006.62.13

Ingrin J, Kohn SC (2008) Water diffusion in forsterite revisited. Geochim Cosmochim Acta 72:S409

Joachim B, Stechern A, Ludwig T, Konzett J, Pawley A, Ruzié-Hamilton L, Clay PL, Burgess R, Ballentine CJ (2017) Effect of water on the fluorine and chlorine partitioning behavior between olivine and silicate melt. Contrib Mineral Petr 172:15. https://doi.org/10.1007/s00410-017-1329-1

Jollands MC, Hermann J, O'Neill HSC, Spandler C, Padrón-Navarta JA (2016a) Diffusion of Ti and some divalent cations in olivine as a function of temperature, oxygen fugacity, chemical potentials and crystal orientation. J Petrol 57:1983–2010. https://doi.org/10.1093/petrology/egw067

Jollands MC, Padrón-Navarta JA, Hermann J, O'Neill HSC (2016b) Hydrogen diffusion in Ti-doped forsterite and the preservation of metastable point defects. Am Mineral 101:1560–1570. https://doi.org/10.2138/am-2016-55681571

Jollands MC, O'Neill HSC, Van Orman J, Berry A, Hermann J, Newville M, Lanzirotti A (2018) Substitution and diffusion of Cr^{2+} and Cr^{3+} in synthetic forsterite and natural olivine at 1200–1500 °C and 1 bar. Geochim Cosmochim Acta 220:407–428. https://doi.org/10.1016/j.gca.2017.09.030

Jollands MC, Kempf E, Hermann J, Müntener O (2019) Coupled inter-site reaction and diffusion: rapid dehydrogenation of silicon vacancies in natural olivine. Geochim Cosmochim Acta 262:220–242. https://doi.org/10.1016/j.gca.2019.07.025

Jollands MC, Zhukova I, O'Neill HSC, Hermann J (2020) Mg diffusion in forsterite from 1250–1600 °C. Am Mineral 105:525–537. https://doi.org/10.2138/am-2020-7286

Jollands MC, O'Neill HSC, Berry AJ, Le Losq C, Rivard C, Hermann J (2021) A combined Fourier transform infrared and Cr K-edge X-ray absorption near-edge structure spectroscopy study of the substitution and diffusion of H in Cr-doped forsterite. Eur J Mineral 33:113–138. https://doi.org/10.5194/ejm-33-113-2021

Jollands MC, Tollan PME, Baumgartner LP, Müntener O (2022) Hydrogen diffusion mechanisms in quartz: insights from H-Li, ^{2}H–H and ^{2}H–H–Li exchange experiments. Mineral Mag 86(1):112–126. https://doi.org/10.1180/mgm.2021.105

Karato SI (1990) The role of hydrogen in the electrical conductivity of the upper mantle. Nature 347:272–273. https://doi.org/10.1038/347272a0

Karato SI, Jung H (1998) Water, partial melting and the origin of the seismic low velocity and high attenuation zone in the upper mantle. Earth Planet Sci Lett 157:193–207. https://doi.org/10.1016/S0012-821X(98)00034-X

Katayama I, Karato SI (2008) Effects of water and iron content on the rheological contrast between garnet and olivine. Phys Earth Planet Inter 166:57–66. https://doi.org/10.1016/j.pepi.2007.10.004

Kempf ED, Hermann J (2018) Hydrogen incorporation and retention in metamorphic olivine during subduction: implications for the deep water cycle. Geology 46:571–574. https://doi.org/10.1130/G40120.1

Kempf ED, Hermann J, Reusser E, Baumgartner LP, Lanari P (2020) The role of the antigorite + brucite to olivine reaction in

subducted serpentinites (Zermatt, Switzerland). Swiss J Geosci 113:16. https://doi.org/10.1186/s00015-020-00368-0

Kohlstedt DL, Mackwell SJ (1998) Diffusion of hydrogen and intrinsic point defects in olivine. Z Phys Chem 207:147–162. https://doi.org/10.1524/zpch.1998.207.Part_1_2.147

Kohlstedt DL, Mackwell S (1999) Solubility and diffusion of "water" in silicate minerals. In: Wright K, Catlow R (eds) Microscopic properties and processes in minerals. Kluwer Academic Publishers, Amsterdam, pp 539–559

Kohlstedt DL, Keppler H, Rubie DC (1996) Solubility of water in the α, β and γ phases of $(Mg, Fe)_2SiO_4$. Contrib Mineral Petrol 123:345–357. https://doi.org/10.1007/s004100050161

Kovács I, O'Neill HSC, Hermann J, Hauri EH (2010) Site-specific infrared O–H absorption coefficients for water substitution into olivine. Am Mineral 95:292–299. https://doi.org/10.2138/am.2010.3313

Kröger FA, Vink HJ (1956) Relations between the concentrations of imperfections in crystalline solids. In: Seitz F, Turnbull D (eds) Solid state physics. Academic Press, Cambridge, pp 307–435. https://doi.org/10.1016/S0081-1947(08)60135-6

Le Losq C, Jollands MC, Tollan PME, Hawkins R, O'Neill HSC (2019) Point defect populations of forsterite revealed by two-stage metastable hydroxylation experiments. Contrib Mineral Petrol 174:53. https://doi.org/10.1007/s00410-019-1590-6

Lemaire C, Kohn S, Brooker R (2004) The effect of silica activity on the incorporation mechanisms of water in synthetic forsterite: a polarised infrared spectroscopic study. Contrib Mineral Petrol 147:48–57. https://doi.org/10.1007/s00410-003-0539-x

Li JP, O'Neill HSC, Seifert F (1995) Subsolidus phase relations in the system $MgO–SiO_2–Cr–O$ in equilibrium with metallic Cr, and their significance for the petrochemistry of chromium. J Petrol 36:107–132. https://doi.org/10.1093/petrology/36.1.107

Li Y, Mackwell SJ, Kohlstedt DL (2022) Diffusion rates of hydrogen defect species associated with site-specific infrared spectral bands in natural olivine. Earth Plan Sci Lett 581:117406. https://doi.org/10.1016/j.epsl.2022.117406

Libowitzky E, Beran A (1995) OH defects in forsterite. Phys Chem Miner 22:387–392. https://doi.org/10.1007/BF00213336

Libowitzky E, Rossman GR (1997) An IR absorption calibration for water in minerals. Am Mineral 82:1111–1115. https://doi.org/10.2138/am-1997-11-1208

Liu H, Zhu Q, Yang X (2019) Electrical conductivity of OH-bearing omphacite and garnet in eclogite: the quantitative dependence on water content. Contrib Mineral Petrol 174:57. https://doi.org/10.1007/s00410-019-1593-3

López Sánchez-Vizcaíno V, Trommsdorff V, Gómez-Pugnaire M, Garrido C, Müntener O, Connolly J (2005) Petrology of titanian clinohumite and olivine at the high-pressure breakdown of antigorite serpentinite to chlorite harzburgite (Almirez Massif, S. Spain). Contrib Mineral Petrol 149:627–646. https://doi.org/10.1007/s00410-005-0678-3

Lu R, Keppler H (1997) Water solubility in pyrope to 100 kbar. Contrib Mineral Petrol 129:35–42. https://doi.org/10.1007/s004100050321

Mackwell SJ, Kohlstedt DL (1990) Diffusion of hydrogen in olivine: implications for water in the mantle. J Geophys Res Solid Earth 95:5079–5088. https://doi.org/10.1029/JB095iB04p05079

Mackwell SJ, Kohlstedt DL, Paterson MS (1985) The role of water in the deformation of olivine single crystals. J Geophys Res Solid Earth 90:11319–11333. https://doi.org/10.1029/JB090iB13p11319

Matveev S, O'Neill HSC, Ballhaus C, Taylor WR, Green D (2001) Effect of silica activity on OH−IR spectra of olivine: implications for low-$aSiO_2$ mantle metasomatism. J Petrol 42:721–729. https://doi.org/10.1093/petrology/42.4.721

McCarty RJ, Stebbins JF (2017) Constraints on aluminum and scandium substitution mechanisms in forsterite, periclase, and larnite: high-resolution NMR. Am Mineral 102:1244–1253. https://doi.org/10.2138/am-2017-5976

Mei S, Kohlstedt DL (2000) Influence of water on plastic deformation of olivine aggregates 1. Diffusion creep regime. J Geophys Res Solid Earth 105:21457–21469. https://doi.org/10.1029/2000JB900179

Moine BN, Bolfan-Casanova N, Radu IB, Ionov DA, Costin G, Korsakov AV, Golovin AV, Oleinikov OB, Deloule E, Cottin JY (2020) Molecular hydrogen in minerals as a clue to interpret ∂D variations in the mantle. Nat Commun 11:3604–3604. https://doi.org/10.1038/s41467-020-17442-8

Monkhorst HJ, Pack JD (1976) Special points for Brillouin-zone integrations. Phys Rev B 13:5188. https://doi.org/10.1103/PhysRevB.13.5188

Muir JMR, Jollands MC, Zhang F, Walker A (2020) Explaining the dependence of M-site diffusion in forsterite on silica activity: a density functional theory approach. Phys Chem Miner 47:55. https://doi.org/10.1007/s00269-020-01123-5

Muir JMR, Zhang F, Walker AM (2021a) The mechanism of Mg diffusion in forsterite and the controls on its anisotropy. Phys Earth Planet Inter 321:106805. https://doi.org/10.1016/j.pepi.2021.106805

Muir JMR, Zhang F, Walker A (2021b) Fast anisotropic Mg and H diffusion in wet forsterite. Earth. https://doi.org/10.31223/X5F63N

Muir JMR, Jollands M, Zhang F, Walker AM (2022) Controls on the distribution of hydrous defects in forsterite from a thermodynamic model. Phys Chem Miner 49(4):7. https://doi.org/10.1007/s00269-022-01182-w

Ni H, Zhang Y (2008) H_2O diffusion models in rhyolitic melt with new high pressure data. Chem Geol 250:68–78. https://doi.org/10.1016/j.chemgeo.2008.02.011

Nielsen RL, Gallahan WE, Newberger F (1992) Experimentally determined mineral-melt partition coefficients for Sc, Y and REE for olivine, orthopyroxene, pigeonite, magnetite and ilmenite. Contrib Mineral Petrol 110:488–499. https://doi.org/10.1007/BF00344083

Novella D, Jacobsen B, Weber PK, Tyburczy JA, Ryerson FJ, Du Frane WL (2017) Hydrogen self-diffusion in single crystal olivine and electrical conductivity of the Earth's mantle. Sci Rep 7:5344. https://doi.org/10.1038/s41598-017-05113-6

O'Neill HSC (1987) Quartz-fayalite-iron and quartz-fayalite-magnetite equilibria and the free energy of formation of fayalite (Fe_2SiO_4) and magnetite (Fe_3O_4). Am Mineral 72:67–75

Oriani RA (1970) The diffusion and trapping of hydrogen in steel. Acta Metall 18:147–157. https://doi.org/10.1016/0001-6160(70)90078-7

Padrón-Navarta JA, Hermann J (2017) A subsolidus olivine water solubility equation for the Earth's Upper Mantle. J Geophys Res Solid Earth 122:9862–9880. https://doi.org/10.1002/2017JB014510

Padrón-Navarta JA, Hermann J, O'Neill HSC (2014) Site-specific hydrogen diffusion rates in forsterite. Earth Planet Sci Lett 392:100–112. https://doi.org/10.1016/j.epsl.2014.01.055

Perdew JP, Burke K, Ernzerhof M (1996) Generalized gradient approximation made simple. Phys Rev Lett 77:3865–3868. https://doi.org/10.1103/PhysRevLett.77.3865

Petersen F (2013) Pressure dependence of Hydrogen Solubility in Olivine type compounds using Fourier Transform Infrared Spectroscopy (FTIR) and Nuclear Reaction Analysis (NRA). Dissertation, Ruhr Universitaet Bochum

Petričević V, Gayen SK, Alfano RR (1988) Laser action in chromium-activated forsterite for near-infrared excitation: is Cr^{4+} the lasing ion? Appl Phys Lett 53:2590–2592. https://doi.org/10.1063/1.100536

Plushkell W, Engell HJ (1968) Ionen und Elektronenleitung in magnesium orthosilikat. Ber Dtsch Keram Ges 45:388

Press WH, Teukolsky SA, Vetterling WT, Flannery BP (2007) Numerical recipes. The art of scientific computing, 3rd edn. Cambridge University Press, Cambridge

Rager H, Taran M, Khomenko V (1991) Polarized optical absorption spectra of synthetic chromium doped Mg_2SiO_4 (forsterite). Phys Chem Miner 18:37–39. https://doi.org/10.1007/BF00199041

Rauch M, Keppler H (2002) Water solubility in orthopyroxene. Contrib Mineral Petrol 143:525–536. https://doi.org/10.1007/s00410-002-0365-6

Robinson K, Gibbs GV, Ribbe PH (1973) The crystal structures of the humite minerals. IV. Clinohumite and Titanoclinohumite. Am Mineral 58:43–49

Smith GD (1985) Numerical solution of partial differential equations: finite difference methods. Oxford University Press, Oxford

Smyth DM, Stocker RL (1975) Point defects and non-stoichiometry in forsterite. Phys Earth Plant Inter 10:183–192. https://doi.org/10.1016/0031-9201(75)90037-0

Spandler C, O'Neill HSC (2010) Diffusion and partition coefficients of minor and trace elements in San Carlos olivine at 1300 °C with some geochemical implications. Contrib Miner Petrol 159:791–818. https://doi.org/10.1007/s00410-009-0456-8

Sun W, Yoshino T, Kuroda M, Sakamoto N, Yurimoto H (2019) H-D interdiffusion in single-crystal olivine: implications for electrical conductivity in the upper mantle. J Geophys Res Solid Earth 124:5696–5707. https://doi.org/10.1029/2019JB017576

Thoraval C, Demouchy S, Padrón-Navarta JA (2019) Relative diffusivities of hydrous defects from a partially dehydrated natural olivine. Phys Chem Miner 46:1–13. https://doi.org/10.1007/s00269-018-0982-x

Tielke JA, Zimmerman ME, Kohlstedt DL (2017) Hydrolytic weakening in olivine single crystals. J Geophys Res Solid Earth 122:3465–3479. https://doi.org/10.1002/2017JB014004

Tollan PME, Smith R, O'Neill HSC, Hermann J (2017) The responses of the four main substitution mechanisms of H in olivine to H_2O activity at 1050 °C and 3 GPa. Progr Earth Planet Sci 4:14. https://doi.org/10.1186/s40645-017-0128-7

Tollan PME, O'Neill HSC, Hermann J (2018) The role of trace elements in controlling H incorporation in San Carlos olivine. Contrib Mineral Petrol 173:89. https://doi.org/10.1007/s00410-018-1517-7

Walker AM, Hermann J, Berry AJ, O'NeillHSC, (2007) Three water sites in upper mantle olivine and the role of titanium in the water weakening mechanism. J Geophys Res Solid Earth 112(B5):B05211

Wan Z, Coogan LA, Canil D (2008) Experimental calibration of aluminum partitioning between olivine and spinel as a geothermometer. Am Mineral 93:1142–1147. https://doi.org/10.2138/am.2008.2758

Wang ZY, Hiraga T, Kohlstedt DL (2004) Effect of H^+ on Fe–Mg interdiffusion in olivine, $(Fe, Mg)_2SiO_4$. Appl Phys Lett 85:209–211. https://doi.org/10.1063/1.1769593

Withers AC, Bureau H, Raepsaet C, Hirschmann MM (2012) Calibration of infrared spectroscopy by elastic recoil detection analysis of H in synthetic olivine. Chem Geol 334:92–98. https://doi.org/10.1016/j.chemgeo.2012.10.002

Yang X, Keppler H, McCammon C, Ni H (2012) Electrical conductivity of orthopyroxene and plagioclase in the lower crust. Contrib Mineral Petrol 163:33–48. https://doi.org/10.1007/s00410-011-0657-9

Yoshino T, Matsuzaki T, Shatskiy A, Katsura T (2009) The effect of water on the electrical conductivity of olivine aggregates and its implications for the electrical structure of the upper mantle. Earth Plan Sci Lett 288:291–300. https://doi.org/10.1016/j.epsl.2009.09.032

Zhang BH, Xia QK (2021) Influence of water on the physical properties of olivine, wadsleyite, and ringwoodite. Eur J Mineral 33:39–75. https://doi.org/10.5194/ejm-33-39-2021

Zhang B, Li B, Zhao C, Yang X (2019) Large effect of water on Fe–Mg interdiffusion in garnet. Earth Plan Sci Lett 505:20–29. https://doi.org/10.1016/j.epsl.2018.10.015

Zhao C, Yoshino T (2016) Electrical conductivity of mantle clinopyroxene as a function of water content and its implication on electrical structure of uppermost mantle. Earth Plan Sci Lett 447:1–9. https://doi.org/10.1016/j.epsl.2016.04.028

Zhukova I, O'Neill HSC, Campbell IH, Kilburn MR (2014) The effect of silica activity on the diffusion of Ni and Co in olivine. Contrib Mineral Petrol 168:1–15. https://doi.org/10.1007/s00410-014-1029-z